Title

Modelling intergranular and transgranular micro-cracking in polycrystalline materials

Authors

Gulizzi, V
Rycroft, CH
Benedetti, I

Publication Date

2018-02-01

DOI

10.1016/j.cma.2017.10.005

Peer reviewed

Available online at www.sciencedirect.com
ScienceDirect
Comput. Methods Appl. Mech. Engrg. 329 (2018) 168–194
Computer methods in applied mechanics and engineering
www.elsevier.com/locate/cma

Modelling intergranular and transgranular micro-cracking in polycrystalline materials

V. Gulizzi[a,b,1], C.H. Rycroft[b,c], I. Benedetti[a,*]

[a] *Dipartimento di Ingegneria Civile, Ambientale, Aerospaziale, dei Materiali - DICAM, Università degli Studi di Palermo, Viale delle Scienze, 90128, Palermo, Italy*
[b] *Paulson School of Engineering and Applied Sciences, Harvard University, Cambridge, MA 02138, USA*
[c] *Mathematics Group, Lawrence Berkeley National Laboratory, Berkeley, CA 94720, USA*

Received 29 June 2017; received in revised form 25 September 2017; accepted 3 October 2017
Available online 14 October 2017

Highlights

- A novel 3D BEM for polycrystalline inter and transgranular cracking competition.
- Inter and transgranular cracking/competition is studied by distinct cohesive laws.
- Cleavage planes nucleation in the grains is based on lattice structure and strength.
- The polycrystalline problem is formulated in terms of intergranular variables only.
- The method allows a reduction of DoFs, appealing for multiscale analysis.

Abstract

In this work, a grain boundary formulation for intergranular and transgranular micro-cracking in three-dimensional polycrystalline aggregates is presented. The formulation is based on the displacement and stress boundary integral equations of solid mechanics and it has the advantage of expressing the polycrystalline problem in terms of grain boundary variables only. The individual grains within the polycrystalline morphology are modelled as generally anisotropic linear elastic domains with random spatial orientation. Transgranular micro-cracking is assumed to occur along specific cleavage planes, whose orientation in space within the grains depend upon the crystallographic lattice. Both intergranular and transgranular micro-cracking are modelled using suitably defined cohesive laws, whose parameters characterise the behaviour of the two mechanisms. The algorithm developed to track the inter/transgranular micro-cracking history is presented and discussed. Several numerical tests involving pseudo-3D and fully 3D morphologies are performed and analysed. The presented numerical results show that the developed formulation is

* Corresponding author.
E-mail addresses: vincenzo.gulizzi@unipa.it (V. Gulizzi), chr@seas.harvard.edu (C.H. Rycroft), ivano.benedetti@unipa.it (I. Benedetti).
[1] On a research leave from the University of Palermo, Italy.

https://doi.org/10.1016/j.cma.2017.10.005
0045-7825/Published by Elsevier B.V.

capable of tracking the initiation and evolution of both intergranular and transgranular cracking as well as their competition, thus providing a useful tool for the study of damage micro-mechanics.
Published by Elsevier B.V.

Keywords: Polycrystalline materials; Transgranular cracking; Intergranular cracking; Micro-mechanics; Cohesive zone modelling; Boundary element method

1. Introduction

In the last few decades, thanks to remarkable advancements in microscopy technologies and high performance computing (HPC), much interest and research have been focused on the study of materials at microscopic scales. Such interest is motivated by various considerations: (a) macroscopic properties of inherently heterogeneous materials naturally depend on the features and interactions of elementary building blocks, or constituents; (b) constitutive phenomenological models may sometimes be overly simplistic or inadequate to represent complex material behaviours, especially when phenomena such as damage nucleation and evolution or phase transformations are present in the considered loading conditions; (c) the knowledge and control of microscopic features may help manufacture materials with enhanced properties.

Such motivations are expressed in the faceted body of investigations addressed at unveiling the so called *structure–property* link for different classes of materials. In such context, computational materials modelling has been assuming increasing importance and the development of more powerful and accessible computational tools and facilities has allowed the inclusion, in various formulations, of details of ever increasing complexity with a clear tendency towards the development of *as realistic as possible* virtual models. As a consequence, multi-scale materials modelling, which aims at bridging different material scales, is today an established scientific paradigm [1].

Polycrystalline materials, which include the majority of metals and ceramics, with several engineering applications, may exemplify the trends sketched above. Polycrystalline materials have been intensely investigated and an increasing level of realism in their virtual modelling has materialised in the transition from two-dimensional (2D) to three-dimensional (3D) models [2], in the representation of more realistic grain morphologies [3], made possible by the use of 3D X-ray diffraction micro-tomography [4], in the inclusion of more sophisticated constitutive behaviour for the grains [5,6] and more sophisticated damage and failure mechanisms [7].

The present paper focuses on modelling of intergranular and transgranular micro-cracking, which represent two of the main failure mechanisms in brittle polycrystalline materials. While intergranular cracking denotes the failure of interfaces between contiguous grains, transgranular cracking refers to the failure of individual bulk grains along specific crystallographic planes. The occurrence of the two cracking modes is affected by several factors such as crystallographic lattice, temperature and the presence of an aggressive environment [8,9]. The crystallographic lattice plays a key role in determining a grain's susceptibility to specific deformation and failure mechanisms. As an example, body-centred cubic (BCC) and hexagonal close packed (HCP) crystals usually show ductile-to-brittle transition at decreasing temperatures [10–12], with inter- and transgranular cracking resulting from the limited number of slip systems in these crystal lattices at low temperatures. On the other hand, although face-centred cubic (FCC) lattices generally favour ductile deformation over a wide range of temperatures as consequence of the large number of slip systems, the action of aggressive environments is well-known to induce grain boundary embrittlement and therefore intergranular and transgranular fracture in naturally ductile materials [13–15]. At room temperature, HPC ceramics, such as 6H silicon carbide (SiC), exhibit inter- and transgranular brittle fracture [16].

Several experimental and numerical studies have been devoted to understanding the complex interaction between inter- and transgranular cracking and their relationship with the morphological, physical and chemical properties of the polycrystalline microstructure. Due to its versatility, several computational studies have been performed within the framework of the finite element method (FEM), employing cohesive zone modelling to capture the damage and fracture propagation in polycrystalline materials exhibiting different constitutive behaviours and subjected to different environmental and loading conditions [17–21].

While in several studies cohesive elements have been extensively used around all the finite elements, aiming at capturing as general as possible crack paths at the expenses of computational effectiveness, Kraft and Molinari [22] developed a 2D FE model in which cohesive interfaces are selectively introduced on-the-fly along specific

crystallographic planes within the crystals, based on a suitable threshold condition on crystallographically resolved stresses, with suitable morphology remeshing.

Transgranular polycrystalline fracture has also been studied using models based on different approaches such as the extended finite element method [23–25], which allows for general crack propagation with limited remeshing only, peridynamics [26] or non-local lattice particle method [27]. Recently, Geraci and Aliabadi [28] presented an integral formulation based on the dual boundary element method and the cohesive zone approach for inter- and transgranular cracking in 2D polycrystalline aggregates.

While several 2D models are present in the literature, few 3D models accounting for the interplay or competition between inter- and transgranular polycrystalline cracking mechanisms have been developed, due to increased geometrical and mechanical complexity and much higher computational requirements. However, the combined effect of inter- and transgranular cracking is an inherently three-dimensional phenomenon, due to the crucial role played by the random crystallographic orientation and therefore the potential cleavage planes within polycrystalline aggregates. Furthermore, as pointed out by some researchers [10–12], 2D model may not be able to fully capture the role of grain boundary fracture in accommodating transgranular crack propagation through misaligned adjacent grains.

Two- and three-dimensional polycrystalline morphologies with inter and transgranular cracking and different constitutive behaviours have been recently studied by some authors using the phase field method [29–34], which offers the advantage of modelling, with relative versatility, the evolution of interfaces representing phase transformations fronts and/or cracks within the aggregate. Three-dimensional modelling of polycrystalline cleavage by cellular automata has also been proposed [35,36].

In this work, the boundary element method is combined with a cohesive zone approach for the study of three-dimensional polycrystalline morphologies undergoing both inter- and trans-granular cracking. To the best of the authors' knowledge, this is the first time a boundary element formulation has been employed to simultaneously address inter and trans-granular cracking within three-dimensional anisotropic crystal aggregates. The boundary element method has been successfully used to study intergranular failure of 2D [37] and 3D [38–41] polycrystalline materials at the grain scale; the above grain-scale intergranular models have also been successfully employed in a multi-scale framework [42,43] for capturing material degradation initiation and evolution at an engineering component level. A 2D model for inter- and transgranular micro-cracking has been recently presented by Geraci and Aliabadi [28]. The boundary element approach allows expressing the polycrystalline problem in terms of grain boundary variables only, thus facilitating the employment of cohesive laws. Here, a new numerical scheme is developed to capture the inter- and transgranular crack propagation in fully 3D polycrystalline materials. The paper is organised as follows: Section 2 presents, after briefly recalling the polycrystalline governing boundary integral equations, the cohesive zone approach employed in this work to model the competition between the inter- and transgranular cracking mechanisms; Section 3 discusses the numerical discretisation of the boundary integral equations and the solution of the system of equations of the entire aggregate. Particular emphasis is given to the proposed algorithm to track the nucleation of transgranular micro-cracks within the considered polycrystalline morphologies; Section 4 presents the numerical results of inter- and transgranular micro-cracking in pseudo 3D and fully 3D polycrystalline morphologies; Section 5 discusses some directions for further research while some conclusions are drawn in Section 6.

2. Grain boundary formulation for polycrystalline microstructures

The features of the grain boundary formulation for intergranular and transgranular micro-cracking in 3D polycrystalline materials are presented in this section.

2.1. Microstructure generation

A polycrystalline microstructure is an aggregate of randomly oriented crystals characterised by their shape, orientation and generally anisotropic properties. The artificial microstructures analysed in this study are represented as 3D Voronoi tessellations, which have been extensively used in the literature as they may satisfactorily reproduce the main statistical features of real polycrystalline aggregates [44–48].

Voronoi tessellations can be generated using open source software packages such as `Voro++` [49] (http://math.lbl.gov/voro++/) or `Neper` [48] (http://neper.sourceforge.net/); in the present work, `Voro++` has been employed both to generate the artificial microstructure and to handle the introduction of transgranular interfaces. As an example, Fig. 1(a) shows a 100-grain hardcore Voronoi tessellation within a cubic box.

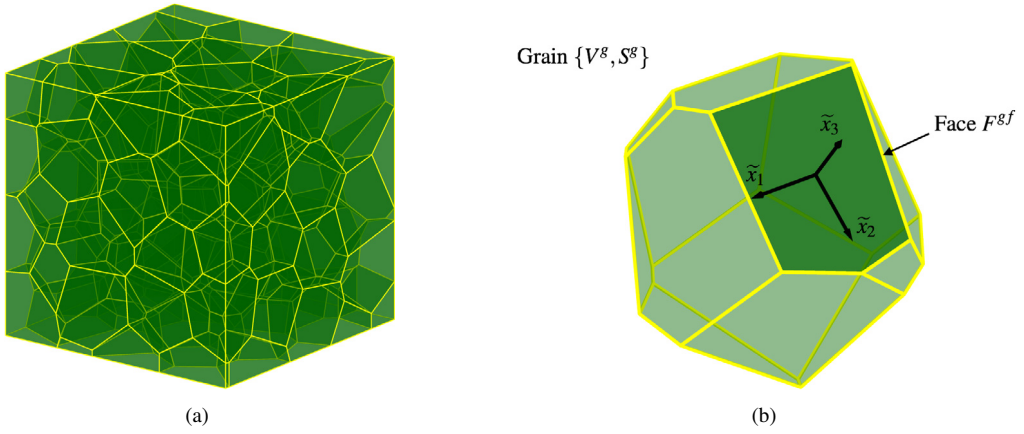

Fig. 1. (a) 100-grain polycrystalline aggregate generated by 100 seeds; (b) Representation of an individual grain highlighting one of its faces in dark green with the attached local reference system $\widetilde{x}_1$-$\widetilde{x}_2$–$\widetilde{x}_3$. (For interpretation of the references to colour in this figure legend, the reader is referred to the web version of this article.)

A tessellation is a collection of N_g grains. The volume occupied by the generic grain g, with $g = 1, \ldots, N_g$, is denoted by V^g. Since Voronoi grains are convex polyhedrons bounded by flat convex polygonal faces, the generic grain boundary is represented as $S^g = \bigcup_{f=1}^{N_f^g} F^{gf}$, being F^{gf} the generic fth face and N_f^g the number of faces of the grain g. Two neighbouring grains share an *interface*, or grain boundary, which is characterised by its own mechanical properties, generally different from those of the two adjacent grains.

Within the polycrystalline microstructure, each grain is characterised by the random orientation of its lattice, which determines its anisotropic mechanical behaviour and the inherently anisotropic features of the cleavage failure mechanisms. In this study, a generic grain g is thus considered as an anisotropic elastic domain, whose constitutive behaviour is expressed by $\sigma_{ij}^g = c_{ijkl}^g \varepsilon_{kl}^g$, where σ_{ij}^g and ε_{ij}^g are components of the second-order stress and strain tensors, respectively, and c_{ijkl}^g are components of the fourth-order elasticity tensor, $i, j, k, l = 1, 2, 3$ and repeated subscripts imply summation.

By virtue of the *integral representation*, Section 2.2, the response of each grain can be written in terms of displacements u_i^g and tractions t_i^g on its boundary S^g.

2.2. Boundary integral equations

The *displacement* boundary integral equations (BIE) governing the behaviour of a generic grain g within the aggregate are

$$\widetilde{c}_{ij}^g(\mathbf{y})\widetilde{u}_j^g(\mathbf{y}) + \int_{S^g} \widetilde{T}_{ij}^g(\mathbf{x}, \mathbf{y})\widetilde{u}_j^g(\mathbf{x})\mathrm{d}S(\mathbf{x}) = \int_{S^g} \widetilde{U}_{ij}^g(\mathbf{x}, \mathbf{y})\widetilde{t}_j^g(\mathbf{x})\mathrm{d}S(\mathbf{x}), \tag{1}$$

where $\mathbf{y}$ and $\mathbf{x} \in S^g$ represent the *collocation* and *integration* points, respectively, and $\widetilde{c}_{ij}^g(\mathbf{y})\widetilde{u}_j^g(\mathbf{y})$ denote the free terms stemming from the boundary limiting process [50,51].

At any internal point $\mathbf{y} \in V^g$ of the grain g, the stress tensor $\sigma_{ij}^g(\mathbf{y})$ can be computed by suitably taking the derivatives of Eq. (1) with respect to the components of $\mathbf{y}$ and using the constitutive relations $\sigma_{ij}^g = c_{ijkl}^g \varepsilon_{kl}^g$. The following *stress* integral equations are obtained:

$$\sigma_{ij}^g(\mathbf{y}) + \int_{S^g} \widetilde{T}_{ijk}^g(\mathbf{x}, \mathbf{y})\widetilde{u}_k^g(\mathbf{x})\mathrm{d}S(\mathbf{x}) = \int_{S^g} \widetilde{U}_{ijk}^g(\mathbf{x}, \mathbf{y})\widetilde{t}_k^g(\mathbf{x})\mathrm{d}S(\mathbf{x}). \tag{2}$$

In Eqs. (1)–(2), the tilde $(\widetilde{\cdot})$ represents components expressed in a surface local reference system. In particular, $\widetilde{u}_i^g$ and $\widetilde{t}_i^g$ represent the boundary displacements and tractions, respectively, expressed in a grain-face-attached local reference system; as an example, the local reference system attached to the fth face of one grain of the tessellation of Fig. 1(a) is showed in Fig. 1(b), where the plane of the interface is indicated by $\widetilde{x}_1$–$\widetilde{x}_2$ and the normal direction is

indicated by $\widetilde{x}_3$. Denoting with $R_{ij}^{gf}(\mathbf{x})$ the transformation matrix that links the global reference system to the local reference system of the fth face of the generic grain g at the point $\mathbf{x}$, the local displacements $\widetilde{u}_i^g(\mathbf{x})$ and tractions $\widetilde{t}_i^g(\mathbf{x})$ are obtained as

$$\widetilde{u}_i^g(\mathbf{x}) = R_{ij}^{gf}(\mathbf{x}) u_j^g(\mathbf{x}), \quad \widetilde{t}_i^g(\mathbf{x}) = R_{ij}^{gf}(\mathbf{x}) t_j^g(\mathbf{x}). \tag{3}$$

The kernels $\widetilde{U}_{ij}^g(\mathbf{x},\mathbf{y})$, $\widetilde{T}_{ij}^g(\mathbf{x},\mathbf{y})$, $\widetilde{U}_{ijk}^g(\mathbf{x},\mathbf{y})$ and $\widetilde{T}_{ijk}^g(\mathbf{x},\mathbf{y})$ can then be written as

$$\begin{aligned} \widetilde{U}_{ij}^g(\mathbf{x},\mathbf{y}) &= U_{ik}^g(\mathbf{x},\mathbf{y}) R_{jk}^{gf}(\mathbf{x}), \quad \widetilde{T}_{ij}^g(\mathbf{x},\mathbf{y}) = T_{ik}^g(\mathbf{x},\mathbf{y}) R_{jk}^{gf}(\mathbf{x}), \\ \widetilde{U}_{ijk}^g(\mathbf{x},\mathbf{y}) &= U_{ijl}^g(\mathbf{x},\mathbf{y}) R_{kl}^{gf}(\mathbf{x}), \quad \widetilde{T}_{ijk}^g(\mathbf{x},\mathbf{y}) = T_{ijl}^g(\mathbf{x},\mathbf{y}) R_{kl}^{gf}(\mathbf{x}), \end{aligned} \tag{4}$$

where $U_{ij}^g(\mathbf{x},\mathbf{y})$, $T_{ij}^g(\mathbf{x},\mathbf{y})$, $U_{ijk}^g(\mathbf{x},\mathbf{y})$ and $T_{ijk}^g(\mathbf{x},\mathbf{y})$ are obtained from the Green's functions of the general anisotropic elastic problem and given in Appendix for the sake of completeness. Similarly, the coefficients $\widetilde{c}_{ij}^g(\mathbf{y})$ of the free terms are given by $\widetilde{c}_{ij}^g(\mathbf{y}) = c_{ik}^g(\mathbf{y}) R_{jk}^{gf}(\mathbf{y})$ where $c_{ij}^g(\mathbf{y}) = \frac{1}{2}\delta_{ij}$ for all points $\mathbf{y} \in S^g$ on a *smooth* surface neighbourhood.

2.3. Intergranular and transgranular cracking modelling

Although intergranular and transgranular cracking are two physically different processes, in the present framework they are modelled employing analogous cohesive laws with different parameters, to account for the different energetic features of the two mechanisms. Cohesive zone modelling [52–55] has been widely used in finite element frameworks [3,56–58] as well as boundary element studies [37,39,40] to model fracture problems.

2.3.1. Intergranular and transgranular failure modes

Intergranular failures occur along the interfaces between contiguous grains, which are generated with the polycrystalline morphology and identify natural sites of crack initiation. Such interfaces are retained during the loading history, even if no intergranular cracking initiates and in general their properties may vary within the aggregate, i.e. the interface between two generic grains a and b may differ from the interface between any other couple of grains c and d.

Transgranular failures, on the contrary, occur *within* the grains, over planes whose position and orientation in space are not *a priori* known. More specifically, different *potential* cleavage planes are uniquely associated with the grain crystallographic lattice; however, a cleavage plane becomes *active*, thus evolving into a transgranular crack surface, only if the corresponding resolved tractions fulfil a defined threshold condition, as given by Eq. (7). In this case, a new flat cracking surface is introduced within the grain, thus forming a new interface whose further evolution is governed by transgranular cohesive parameters. In this work, it is assumed that, once started, transgranular failure evolves over a surface whose envelope lies over a plane; this assumption is justified by experimental observations on several classes of metallic [12,59–61] and ceramic materials [62].

It is worth noting that, once the damaging process is initiated, intergranular and transgranular cracks are analogously treated from the algorithmic/computational point of view, differing only for the values of the cohesive parameters. For the sake of clarity, in this section, the grain boundary quantities referring to an interface $\mathscr{I}^{gh}$ between two different contiguous grains g and h are denoted by the superscript gh. On the other hand, the quantities relating to a cleavage plane within the grain g are denoted by the superscript g only, since they refer to the properties of the bulk grain g. As an example, Fig. 2(a) shows a grain boundary interface between two adjacent grains, whereas Fig. 2(b) shows a potential transgranular interface identified by a specific crystallographic plane passing through the point $\mathbf{y}$ within a bulk grain.

2.3.2. Crack initiation criteria

In the intergranular case, the damage initiation is naturally expressed in terms of intergranular tractions. Damage is initiated at the interface $\mathscr{I}^{gh}$ when

$$\tau_e^{gh} = \sqrt{\left\langle \tau_n^{gh} \right\rangle^2 + \left(\frac{\beta^{gh}}{\alpha^{gh}} \tau_s^{gh} \right)^2} > T_{\max}^{gh}, \tag{5}$$

where τ_e^{gh} is an effective intergranular traction [37,39], $\tau_s^{gh} = \sqrt{(\widetilde{t}_1^{gh})^2 + (\widetilde{t}_2^{gh})^2}$ is the traction along the sliding direction, $\tau_n = \widetilde{t}_3^{gh}$ is the traction along the normal direction and $T_{\max}^{gh}$ is the intergranular cohesive strength, which

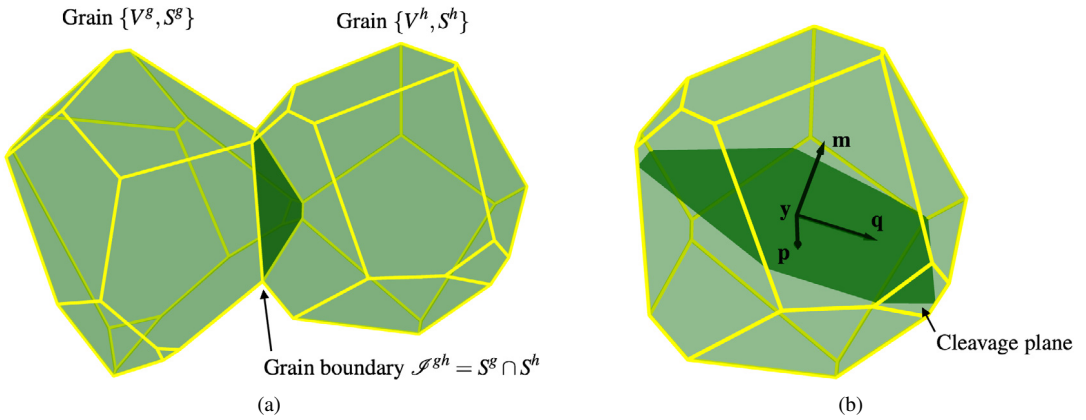

Fig. 2. (a) Detail of two contiguous grains of the tessellation of Fig. 1(a) showing their shared interface, which is highlighted with dark green; (b) Potential cleavage plane (in dark green) passing through the point **y**. The local reference system of the cleavage plane is denoted by the unit normal **m** and by two mutually orthogonal unit vectors **p** and **q**. (For interpretation of the references to colour in this figure legend, the reader is referred to the web version of this article.)

may assume different values over different interfaces. α^{gh} and β^{gh} are cohesive parameters weighting the relative influence of mode I and II cracking and are also used in the cohesive laws given in Eqs. (9)–(10).

In the transgranular case, a similar initiation threshold is defined *with reference to the potential cleavage planes passing through the control points scattered within the grain volume*. In particular, for a generic control point $\mathbf{y} \in V^g$, the stress tensor $\sigma_{ij}^g(\mathbf{y})$ is computed by using the stress boundary integral equation, Eq. (2), and it is projected onto the potential cleavage planes to define the normal τ_n^g and tangential $\tau_s^g = \sqrt{(\tau_p^g)^2 + (\tau_q^g)^2}$ tractions, with

$$\tau_n^g = m_i^g \sigma_{ij}^g m_j^g, \qquad \tau_p^g = p_i^g \sigma_{ij}^g m_j^g, \qquad \tau_q^g = q_i^g \sigma_{ij}^g m_j^g, \tag{6}$$

where m_i^g is the unit normal associated with the potential cleavage plane and p_i^g and q_i^g are two mutually orthogonal directions lying on the plane itself, as shown in Fig. 2(b); These resolved tractions then enter the definition of the effective traction τ_e^g used in the threshold criterion

$$\tau_e^g = \sqrt{\langle \tau_n^g \rangle^2 + \left(\frac{\beta^g}{\alpha^g} \tau_s^g \right)^2} > T_{\max}^g, \tag{7}$$

where α^g and β^g are the values of the cohesive law coefficients characterising the cohesive behaviour of the transgranular cracks and $T_{\max}^g$ is the *cleavage plane strength*, which may assume different values for cleavage with different lattice orientations. At a specific load increment, the values of the effective stress τ_e^g are computed for each potential cleavage plane at each control point and Eq. (7) is assessed; in this way, the most loaded cleavage system is identified and a transgranular cohesive interface is introduced into the grain as a flat surface extending up to the boundaries of the grain.

2.3.3. Cohesive traction–separation laws

When damage is initiated, a strong discontinuity is introduced in the model and *extrinsic* cohesive laws [54,55] of the form

$$\widetilde{t}_i^x = C_{ij}(d^*)\, \delta \widetilde{u}_j^x \qquad (i = 1, 2, 3) \tag{8}$$

are used to link the boundary traction components $\widetilde{t}_i^x$ with the boundary displacements jump $\delta \widetilde{u}_i^x$ across the discontinuity where, consistently with the notation introduced in Eqs. (1)–(2) and Section 2.3.1, the tilde $(\widetilde{\cdot})$ denotes quantities expressed in the *local* reference systems and $x = gh$ or $x = g$, depending on whether an intergranular or transgranular discontinuities are being considered.

The constitutive constants $C_{ij}(d^*)$ are given as a function of an *irreversible damage parameter* $d^* = \max_{\mathscr{H}_d}\{d\} \in [0, 1]$ where $\mathscr{H}_d$ is the load history and d is a dimensionless *effective opening displacement* defined as

$$d = \sqrt{\left\langle \frac{\delta\widetilde{u}_n}{\delta u_n^{cr}} \right\rangle^2 + \left(\beta \frac{\delta\widetilde{u}_s}{\delta u_s^{cr}} \right)^2}, \tag{9}$$

where $\delta\widetilde{u}_s = \sqrt{\delta\widetilde{u}_1^2 + \delta\widetilde{u}_2^2}$ and $\delta\widetilde{u}_n = \delta\widetilde{u}_3$ are the sliding and normal displacement jumps, respectively, δu_s^{cr} and δu_n^{cr} are the corresponding critical values at which pure interface opening or pure interface sliding failure occurs, β is a coefficient weighing the normal and sliding modes and $\langle\cdot\rangle = \max(0, \cdot)$ are Macauley brackets.

Assuming no coupling between normal opening and relative sliding and isotropic behaviour with respect to sliding over the discontinuity surface, the constants $C_{ij}(d^*)$ can be written as $C_{ij}(d^*) = \text{diag}\{C_s(d^*), C_s(d^*), C_n(d^*)\}$, where [39]

$$C_s(d^*) = \alpha \frac{T_{\max}}{\delta u_s^{cr}} \frac{1 - d^*}{d^*}, \quad C_n(d^*) = \frac{T_{\max}}{\delta u_n^{cr}} \frac{1 - d^*}{d^*}, \tag{10}$$

where α is a constant chosen so as to ensure a desired ratio between mode II and mode I fracture energies G_{II}/G_I. The cohesive law is fully defined by the cohesive strength $T_{\max}$, the fracture energy G and the relative contribution between opening and sliding failure modes. It is worth noting that as long as the interface remains pristine with $d^* = 0$, Eqs. (8) simply enforce zero displacement jumps, $\delta\widetilde{u}_i^x = 0$, and traction equilibrium. The interested reader is referred to Refs. [39,40] for further details about the considered traction–separation law in the context of the grain boundary formulation for polycrystalline mechanics.

It is noted here that both displacement jumps and tractions directly enter the formulation as primary variables whose values are determined coupling the displacements boundary integral equations (1), written for each grain of the aggregate, with the interface equations.

2.3.4. Inter/transgranular mode competition

The competition between the inter- and transgranular modes of failure in polycrystalline materials is modelled by considering suitable sets of parameters entering the corresponding cohesive laws. Here it is assumed that the coefficients α and β and the ratio G_{II}/G_I do not differ between the two mechanisms, i.e. $\alpha^{gh} = \alpha^g = \alpha$, $\beta^{gh} = \beta^g = \beta$ and $G_{II}^{gh}/G_I^{gh} = G_{II}^g/G_I^g \; \forall g = 1, \ldots, N_g$ and $\forall gh = 1, \ldots, N_i$, being N_g the number of grains and N_i the number of grain boundary interfaces. However, different ratios between the mode I fracture energy G_I^{gh} of the grain boundaries and the mode I fracture energy G_I^g of the cleavage planes are considered.

More specifically, considering that the work of separation can be written using the relation $G_I = T_{\max}\delta u_n^{cr}/2$, it is observed that the ratio $\gamma_G \equiv G_I^g/G_I^{gh}$ between the two aforementioned fracture energies can be modified by changing $T_{\max}$ and/or δu_n^{cr}. In this work, to scale the fracture energy G_I^g of the factor γ_G, i.e. $G_I^g = \gamma_G G_I^{gh}$, it is assumed that both the interface strength $T_{\max}$ and the critical displacement δu_n^{cr} in mode I are scaled by the same amount, i.e. $T_{\max}^g = \sqrt{\gamma_G} \cdot T_{\max}^{gh}$ and $\delta u_n^{cr,g} = \sqrt{\gamma_G} \cdot \delta u_n^{cr,gh}$. In the same way, it is possible to verify that the critical displacement δu_s^{cr} in mode II is scaled by $\sqrt{\gamma_G}$, i.e. $\delta u_s^{cr,g} = \sqrt{\gamma_G} \cdot \delta u_s^{cr,gh}$.

This is just a particular choice for weighting the two failure mechanisms in order to perform some systematic parametric analysis, but other choices are possible; indeed, the model allows selecting completely unrelated cohesive laws for modelling the two mechanisms. The effect of such a selection of the parameter γ_G on the cohesive law is represented in Fig. 3. Fig. 3(a) represents the tangential component τ_s as a function of $(\beta\delta u_s/\delta u_s^{cr})$ and $(\delta u_n/\delta u_n^{cr})$ whereas Fig. 3(b) represents the normal component τ_n as a function of $(\beta\delta u_s/\delta u_s^{cr})$ and $(\delta u_n/\delta u_n^{cr})$ obtained using Eqs. (8) and (10). In the figures, the red surfaces represent a reference cohesive law, e.g. that associated with the behaviour of the grain boundaries, whereas the blue surfaces represent a scaled cohesive law with $\gamma_G < 1$.

3. Numerical discretisation

Polycrystalline inter- and transgranular micro-cracking is numerically studied discretising Eqs. (1)–(2). The boundary S^g of the generic grain g is subdivided into non-overlapping elements according to the meshing strategy developed in Ref. [40], where triangular and quadrangular, continuous and semi-discontinuous elements were used to reduce the computational cost of the polycrystalline problems. The mesh size s_{ms} of the surface mesh is chosen so that the average element length l_e is much smaller than the cohesive zone size L_{cz}, which can be estimated in

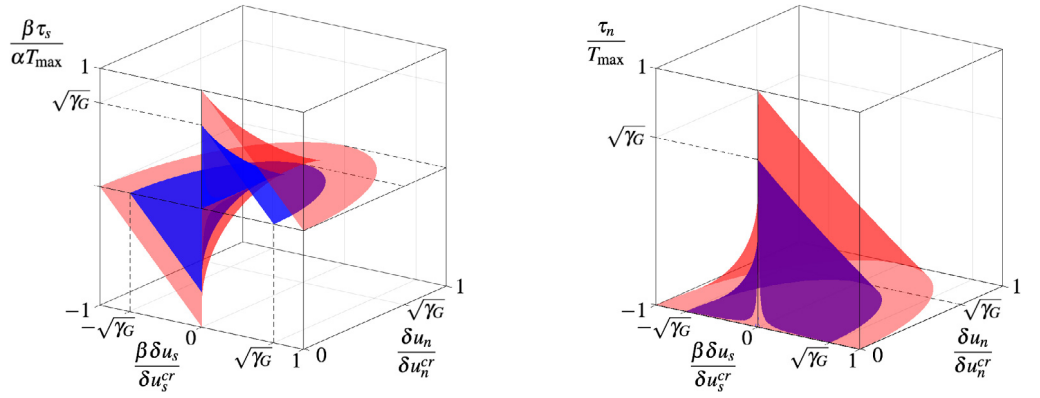

Fig. 3. Schematic representation of the (a) tangential and (b) normal components of the two cohesive laws used to model inter- and transgranular cracking. The red surfaces represent a reference cohesive law, whereas the blue surfaces represent a scaled cohesive law with $\gamma_G < 1$. (For interpretation of the references to colour in this figure legend, the reader is referred to the web version of this article.)

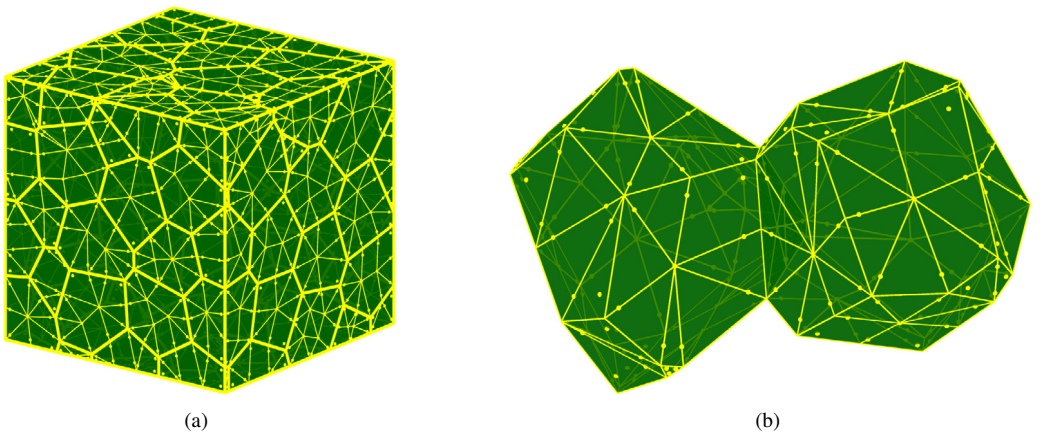

Fig. 4. (a) Mixed triangular/quadrangular surface mesh of the polycrystalline aggregate shown in Fig. 1(a). (b) Detail of the surface mesh of the grains shown in Fig. 2. The small dots in the figures denote the position of the collocation nodes.

terms of the material fracture toughness and the interface strength [57,58,63]. Fig. 4(a) shows the surface mesh of the polycrystalline morphology in Figs. 1(a) and 4(b) shows the surface mesh of the two grains of Fig. 1. In the figures, the small dots denote the collocation points.

The discrete algebraic version of the displacement and stress boundary integral equations is built using the assembly techniques of the standard boundary element method [51]. The boundary displacements u_i and tractions t_i are approximated over each grain boundary mesh element using linear triangular and quadrangular shape functions in conjunction with element's nodal values. The displacement BIEs (1) are then written for every collocation point y of the boundary mesh of each grain and are numerically integrated leading to a linear system of the form

$$\boldsymbol{H}^g \boldsymbol{U}^g = \boldsymbol{G}^g \boldsymbol{T}^g, \tag{11}$$

where the matrices $\boldsymbol{H}^g$ and $\boldsymbol{G}^g$ are obtained by integrating the product of the kernels T_{ij}^g and U_{ij}^g, respectively, by the shape functions and the Jacobian over the surface mesh of the grain g, and the vectors $\boldsymbol{U}^g$ and $\boldsymbol{T}^g$ collect the nodal values of the boundary displacements and tractions, respectively.

Unlike the displacement BIE, which are evaluated on the boundary of the grains, the stress boundary integral equations (2) are evaluated at selected *internal control points*. In the simplest case, the control point can be chosen

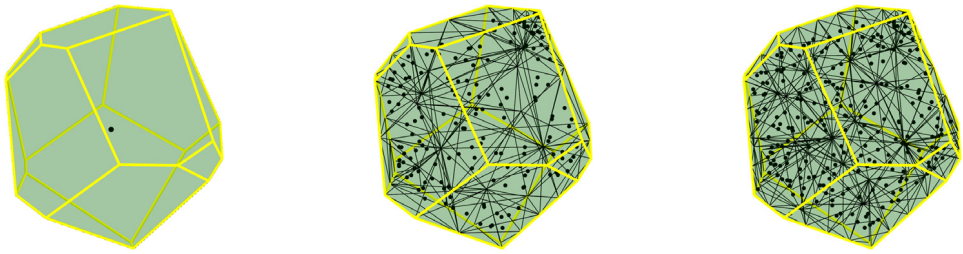

(a) (b) (c)

Fig. 5. Distribution of the control points (denoted by black dots) used to compute the stress tensor σ_{ij} inside a generic grain: (a) in this case, the centroid of the grain is chosen as control point; (b) , (c) distribution of the control points for two different values of the volume mesh size v_{ms}.

as coincident with the centroid of the grain as shown in Fig. 5(a). On the other hand, the control points can also be obtained by generating a volume tetrahedral mesh of each grain and then selecting the centroids of the tetrahedrons. The size of the mesh is controlled by an average volume mesh size v_{ms}, which can be adjusted independently of the average surface mesh size. Fig. 5(b) and 5(c) show two different sets of control points for two different values of the volume mesh size v_{ms}. In the figures, the control points are indicated by the black dots.

Given the position of the volume control points, the stress tensor inside each grain is expressed as a function of the boundary displacements and tractions by means of the following discretised version of Eq. (2):

$$\boldsymbol{\Sigma}^g = \boldsymbol{G}^g_\sigma \boldsymbol{T}^g - \boldsymbol{H}^g_\sigma \boldsymbol{U}^g, \tag{12}$$

where the matrices $\boldsymbol{H}^g_\sigma$ and $\boldsymbol{G}^g_\sigma$ are obtained by integrating the product of the shape functions, the Jacobians and the kernels T^g_{ijk} and U^g_{ijk}, respectively, over the surface mesh of the grain g, and the vector $\boldsymbol{\Sigma}^g$ collects the components of the stress tensor σ^g_{ij} at the volume control points. It is worth noting that, if n^g_v is the number of control points for the grain g and the stress tensor is represented in Voigt notation, the matrices $\boldsymbol{H}^g_\sigma$ and $\boldsymbol{G}^g_\sigma$ have $6n^g_c$ rows and $3n^g_s$ columns, being n^g_s the number of collocation points of the grain g.

3.1. Boundary conditions

Eq. (11) is reordered according to the unknown and known values of grain boundary displacements and tractions [38–40]. The known values are given by the boundary conditions that are enforced over the external faces of the aggregate and are usually expressed as a function of a load factor λ governing the loading history. Eq. (11) can then be rewritten as

$$\boldsymbol{A}^g \boldsymbol{X}^g = \boldsymbol{C}^g \boldsymbol{Y}^g(\lambda), \tag{13}$$

where $\boldsymbol{X}^g$ and $\boldsymbol{Y}^g$ collect the unknown and known values, respectively, of the boundary displacements and tractions of the grain g and the matrices $\boldsymbol{A}^g$ and $\boldsymbol{C}^g$ collect suitably reordered columns from the matrices $\boldsymbol{H}^g$ and $\boldsymbol{G}^g$.

3.2. Polycrystalline system assembly

The overall system of the polycrystalline aggregate is obtained by writing Eq. (13) for each grain of the aggregate and enforcing the interface equations at the grain boundaries. The resulting system can be written as [40]

$$\boldsymbol{M}(\boldsymbol{X}, \lambda, \mathscr{H}) = \begin{Bmatrix} \boldsymbol{A}\boldsymbol{X} - \boldsymbol{B}(\lambda) \\ \boldsymbol{I}(\boldsymbol{X}, \mathscr{H}) \end{Bmatrix} = \boldsymbol{0}, \tag{14}$$

where

$$\boldsymbol{A} = \begin{bmatrix} \boldsymbol{A}^1 & \boldsymbol{0} & \cdots & \boldsymbol{0} \\ \boldsymbol{0} & \boldsymbol{A}^2 & \cdots & \boldsymbol{0} \\ \vdots & \vdots & \ddots & \vdots \\ \boldsymbol{0} & \boldsymbol{0} & \dots & \boldsymbol{A}^{N_g} \end{bmatrix}, \quad \boldsymbol{B} = \begin{Bmatrix} \boldsymbol{C}^1\boldsymbol{Y}^1 \\ \boldsymbol{C}^2\boldsymbol{Y}^2 \\ \vdots \\ \boldsymbol{C}^{N_g}\boldsymbol{Y}^{N_g} \end{Bmatrix}, \quad \boldsymbol{X} = \begin{Bmatrix} \boldsymbol{X}^1 \\ \boldsymbol{X}^2 \\ \vdots \\ \boldsymbol{X}^{N_g} \end{Bmatrix} \tag{15}$$

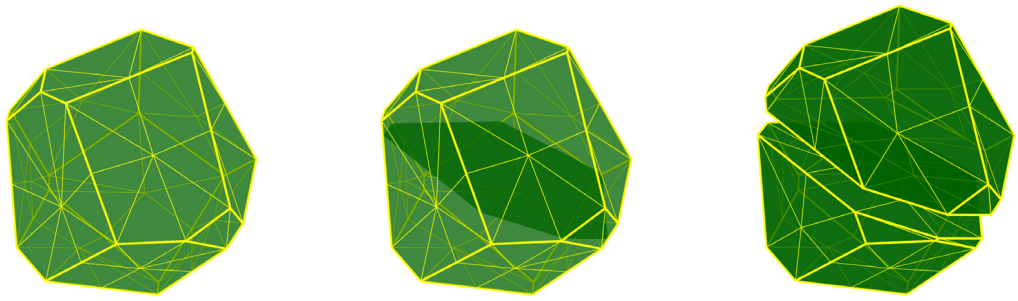

Fig. 6. (a) Boundary mesh of a grain at the point of undergoing cleavage cracking; (b) cleavage plane (in darker green) that needs to be introduced into the grain; (c) mesh of the two child grains originated from the grain in figure (a). (For interpretation of the references to colour in this figure legend, the reader is referred to the web version of this article.)

and $\boldsymbol{I}(\boldsymbol{X}, \mathscr{H})$ implements the interface equations, including continuity, cohesive, frictional contact intergranular equations [39], which generally involve the grain boundaries displacements and tractions and depend on the loading history $\mathscr{H}$.

3.3. Polycrystalline system solution

The system of equations given in (14) must be solved at each load step of the loading history. However, unlike the previous studies [39,40] on the intergranular fracture of polycrystalline materials, at each load step the occurrence of transgranular cracking is considered. The algorithm for inter- and transgranular cracking in polycrystalline materials is detailed in the following section.

3.3.1. Representation of the polycrystalline morphology

The polycrystalline morphology is computed using the `Voro++` software library. `Voro++` stores each Voronoi cell as an irregular convex polyhedron, each with a unique numerical ID, and containing information about vertex positions and edges. In addition, each face stores the ID of the neighbouring grain that it touches.

When transgranular cracking occurs it is necessary to split a grain into two. As an example, Fig. 6(a) shows a grain and its boundary mesh, and Fig. 6(b) shows a cleavage plane through the grain. The `Voro++` library has a standard function that can recompute a polyhedron after intersection with a half-space. To split the grain, it is copied into two, and half-space intersections with opposite signs are applied to the two copies. After recomputing boundary meshes for the new grain shapes, this results in Fig. 6(c).

In addition, for each grain face that was split in two, the corresponding face of the neighbouring grain is split into two faces by introducing an extra edge across it. The neighbour ID information for the two new faces is updated to reference the IDs of the two new split grains. The `Voro++` library was extended to perform this operation. The extension also works when a grain is successively split multiple times, which requires multiple new edges to be introduced in the neighbouring grain faces.

3.3.2. Algorithm for inter- and transgranular cracking

Fig. 7 schematises the algorithm used in the present work to address inter- and transgranular cracking in polycrystalline materials. At the beginning of the analysis, the load factor λ is initialised to 0, the load step counter n is initialised to 1 and the *remesh* Boolean variable is initialised to `false`. The polycrystalline morphology is then generated and the properties of the constituent grains and grain boundaries are loaded. The algorithm then enters the incremental loop that is governed by the counter n and can be described by the following steps:

1. At the beginning of the load step n, the load factor is incremented with the increment $\Delta\lambda_n$ chosen based on the number of iterations needed to reach convergence at the previous load step as in [39]. Moreover, the increment $\Delta\lambda_n$ is always bounded by a lower increment $\Delta\lambda_{\min}$, which is chosen to avoid stagnation of the solution and on the basis of the final value λ_f of the load factor.

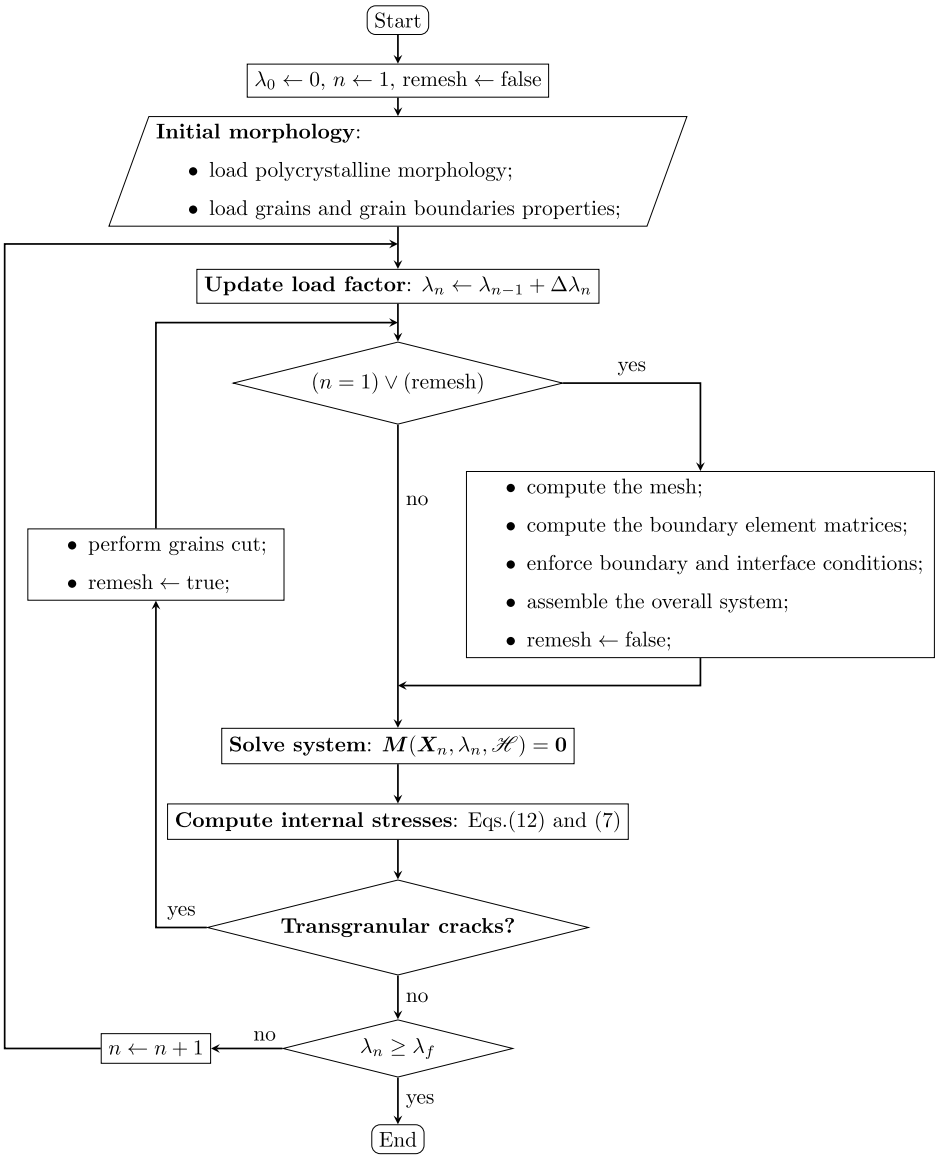

Fig. 7. Flow chart of the algorithm for inter- and transgranular cracking.

2. If the analysis has just started, i.e. $n = 1$, or the remesh is `true`, the aggregate is discretised, the boundary element matrices appearing in Eqs. (13) and (12) are computed and stored, the overall element system given in (14) is then assembled and the remesh variable is set to `false`. It is worth noting that if the algorithm reaches this step after trans-granular cracking has occurred, the previously computed boundary element matrices are discarded and the last computed solution is mapped onto the new mesh.
3. At the nth load step, the system of equation $\boldsymbol{M}(\boldsymbol{X}_n, \lambda_n, \mathscr{H}) = \boldsymbol{0}$, see Eq. (14), is solved [40]. The equilibrium solution $\boldsymbol{X}_n$ is obtained by employing the Newton–Raphson algorithm. It is worth noting the system of equations given in (14) consists of a set of linear equations and a set of nonlinear equations represented by $\boldsymbol{A}\boldsymbol{X} - \boldsymbol{B}(\lambda) = \boldsymbol{0}$ and $\boldsymbol{I}(\boldsymbol{X}, \mathscr{H}) = \boldsymbol{0}$, respectively. As a consequence, the part of the Jacobian matrix of the system corresponding to the linear set of equations is computed at the beginning of the analysis and kept fixed during the Newton–Raphson search for the solution. On the other hand, the part of the Jacobian matrix of the system corresponding

to the nonlinear set of equations, i.e. the interface equations, are updated at each iteration of the Newton–Raphson algorithm on the basis of the interface status. In fact, during the Newton–Raphson search for the solution, the consistency of the grains interfaces and their status, i.e. continuity, cohesive and/or frictional contact, is checked according to the procedure described in Ref. [39].
Furthermore, since the Jacobian of the system is highly sparse, the library `PARDISO` [64–66] (http://www.pardiso-project.org) combining both direct and iterative solution methods is used as a solver. In particular, upon noting that between successive loading steps and/or Newton–Raphson iterations the changes in the Jacobian matrix might be small, the LU factorisation at one step might be used for preconditioning the iterative solution of the subsequent system of equations. In case that the iteration convergence is not reached, the solver automatically switches to the direct numerical factorisation.

4. The values of the stress tensor σ_{ij}^g at the control points of each grain of the aggregate is computed by means of Eq. (12) and the possible occurrence of transgranular cracking is then checked by comparing the local resolved cleavage stress τ_e^g, computed using Eq. (7), with the local threshold value $T_{\max}^g$.
5. If the cleavage threshold is overcome, a new cohesive interface must be introduced following the procedure described in Section 3.3.1. It is worth noting that the transgranular threshold condition may be achieved at multiple points within the morphology. However, since such a solution represents a temporary solution that must be recomputed, only one transgranular interface is introduced. Such interface is that corresponding to the highest value of the difference between the local resolved cleavage stress τ_e^g and the threshold value $T_{\max}^g$. The cohesive properties are those corresponding to transgranular cracks and are in general different from the cohesive properties at the grain boundaries. The cleavage of the grain and the recomputation of the boundary meshes are performed as in Section 3.3.1. At this point, the morphology has been modified and the boolean variable remesh is set to `true`. The flow goes back to step 2 in order to find the equilibrium solution of the new aggregate for the same load factor λ_n.
It is worth noting that the algorithm keeps adding transgranular interfaces as long as the local value of the local resolved cleavage stress τ_e^g is above $T_{\max}^g$. The next loading step is considered when the condition $\tau_e^g < T_{\max}^g$ is fulfilled at all the control points of the morphology.
6. If no transgranular cracks are introduced, the current load factor λ_n is compared to the final load factor λ_f and either the next load step is considered or the analysis is terminated.

4. Computational tests

In this study, polycrystalline SiC aggregates with hexagonal crystal lattice are considered. For hexagonal 6H SiC polytypes, the preferred cleavage plane is the basal plane [31] identified by (0001) Miller indices. The elastic properties of the crystals and the cohesive properties of the grain boundaries and the cleavage planes are listed in Table 1. In the table, the fracture toughness ratio γ_G is varied during the analyses to weigh the effect of inter- and transgranular failure mechanisms in polycrystalline SiC aggregates.

In this section, two sets of tests are discussed. First, the consistency of the proposed numerical scheme is assessed by studying the inter- and transgranular response of pseudo-3D morphologies with columnar grains. Then, the scheme is employed to investigate the inter- and transgranular response of fully 3D morphologies under different loading conditions and different values of the fracture toughness ratio γ_G.

4.1. Pseudo-3D (columnar) morphologies

Fig. 8 shows a pseudo-3D 50-grain morphology with ASTM grain size $G = 12$, subject to tensile strain and in presence of an initial crack originating on the left wall of the aggregate. A uniform displacement $u_3 = \lambda/2$ and $u_3 = -\lambda/2$ is prescribed on the top and bottom faces whereas on the lateral surfaces the boundary conditions are set to $u_i n_i = 0$ being n_i the unit normal of the surfaces. No shear traction act on the external walls. For this set of tests, the morphology shown in Fig. 8 has been meshed using three different mesh sizes s_{ms} shown in Fig. 9. Following [38], the surface mesh size s_{ms} is controlled by means of a density mesh parameter d_m defined in terms of the average length of the grain edges. Fig. 9 also shows the position of the volume control points computed as the centroids of a tetrahedral volume mesh with a volume mesh size equal to $v_{ms} = 2\ \mu\text{m}$.

Table 1
Elastic and cohesive properties of SiC polycrystalline aggregates.

Domain	Property	Component	Value
Bulk crystals	Elastic constants [10^9 N/m^2]	c_{1111}, c_{2222}	502
		c_{3333}	565
		c_{1122}	95
		c_{1133}, c_{2233}	96
		c_{2323}, c_{1313}	169
		c_{1212}	$(c_{1111} - c_{1122})/2$
Grain boundaries	Interface strength [MPa]	$T^{gh}_{\max}$	500
	Cohesive law constants [–]	α^{gh}	1
		β^{gh}	$\sqrt{2}$
	Critical displacements jumps [μm]	$\delta u_n^{cr,gh}$	$7.8089 \cdot 10^{-2}$
		$\delta u_s^{cr,gh}$	$1.5618 \cdot 10^{-1}$
Cleavage planes	Interfacestrength [MPa]	$T^{g}_{\max}$	$\sqrt{\gamma_G} \cdot T^{gh}_{\max}$
	Cohesive law constants [–]	α^{g}	α^{gh}
		β^{g}	β^{gh}
	Critical displacements jumps [μm]	$\delta u_n^{cr,g}$	$\sqrt{\gamma_G} \cdot \delta u_n^{cr,gh}$
		$\delta u_s^{cr,g}$	$\sqrt{\gamma_G} \cdot \delta u_s^{cr,gh}$

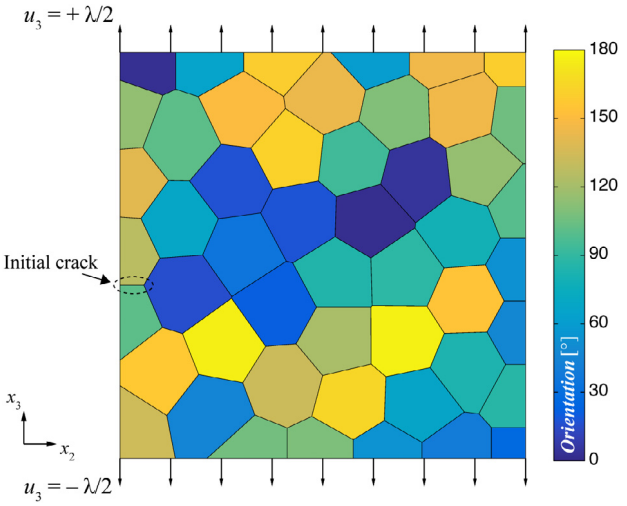

Fig. 8. 50-grain pseudo-3D (columnar) morphology with ASTM grain size $G = 12$ subject to prescribed values of vertical displacements u_3 on top and bottom faces. The colourmap indicates the orientation of the grains with respect to the loading x_2 axis. The initial crack on the left face of the aggregate is circled and highlighted in red. (For interpretation of the references to colour in this figure legend, the reader is referred to the web version of this article.)

In this set of pseudo-3D tests, the fracture toughness ratio γ_G is set to $\gamma_G = 1/4$. Fig. 10 shows the curves of macroscopic stress Σ_{33} versus load factor λ for the different mesh sizes. The figures show that the macroscopic curves satisfactorily overlap and the difference in the maximum computed stress of the two fine meshes is around 2%. Moreover, the three different meshes predict the same micro-crack pattern, which is shown in Fig. 11 for different values of the load factor. More specifically, Fig. 11(a) shows the occurrence of the first transgranular crack at the tip of the pre-existing crack; Fig. 11(b) and 11(c) show the crack pattern at two consecutive load steps; Fig. 11(b) shows the damage distribution at the maximum value of the computed macroscopic stress Σ_{33} whereas, as softening initiates, it is interesting to note that the next equilibrium condition is found after the transgranular crack propagates through three consecutive grains; Fig. 11(d) shows how the crack switches from transgranular to intergranular mode due to the local orientation of the grains, see Fig. 8; eventually, Fig. 11(e) shows the fully developed crack path.

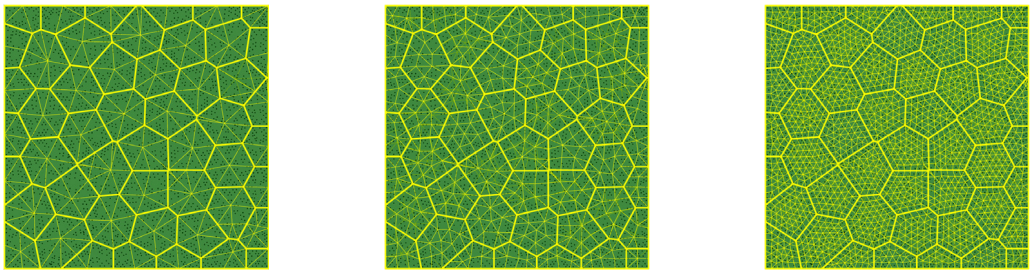

Fig. 9. Three different meshes of the morphology shown in Fig. 8: (a) $s_{ms} = 4$ µm, (b) $s_{ms} = 2$ µm, (c) $s_{ms} = 1$ µm.

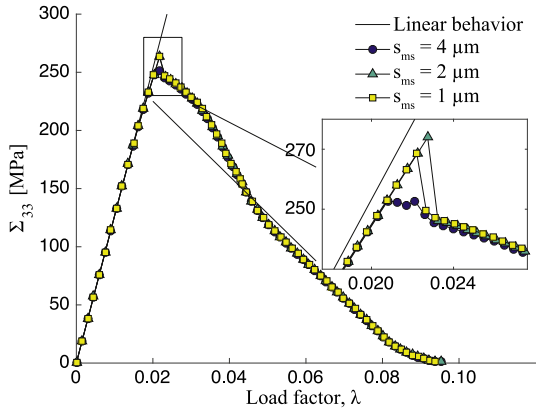

Fig. 10. Macroscopic stress averages Σ_{33} as a function of the load factor λ and the different mesh sizes.

The fully developed crack path is also shown in Fig. 12(a), where the grains are coloured according to their susceptibility to transgranular cracking. Such *transgranular susceptibility index* is computed using the relation

$$TG(\theta) = \left| \frac{\theta - \pi/2}{\pi/2} \right|, \tag{16}$$

where $\theta - \pi/2$ represents the difference between the local grain orientation θ and the *loading* direction $\pi/2$. Similarly, Fig. 12(b) shows the effect of changing the orientation of one grain on the final crack pattern. In particular, changing the orientation of the grain circled in Fig. 12 has the effect of impeding the transgranular crack propagation and it modified the final crack pattern.

4.2. 3D morphologies

The first set of tests are carried out to assess the effect of the mesh size on the inter- and transgranular crack propagation in fully 3D polycrystalline morphologies. Fig. 13(a) shows a 3D 50-grain cubic morphology with ASTM grain size $G = 12$ subject to tensile strain and in presence of an initial crack, which is highlighted in red in the figure. Similarly to the pseudo-3D tests, a uniform displacement $u_3 = \lambda/2$ and $u_3 = -\lambda/2$ is prescribed on the top and bottom faces whereas, on the lateral surfaces, the boundary conditions are set to $u_i n_i = 0$. The external shear traction are zero everywhere.

The three different meshes and the volume control points are reported in Fig. 13(b)–(c). The fracture toughness ratio γ_G is set to $\gamma_G = 1/4$. Fig. 14(a) shows the curves of macroscopic stress Σ_{33} as a function of the load factor λ and the different mesh sizes. The figure shows that the macroscopic curves corresponding to $s_{ms} = 3$ µm and

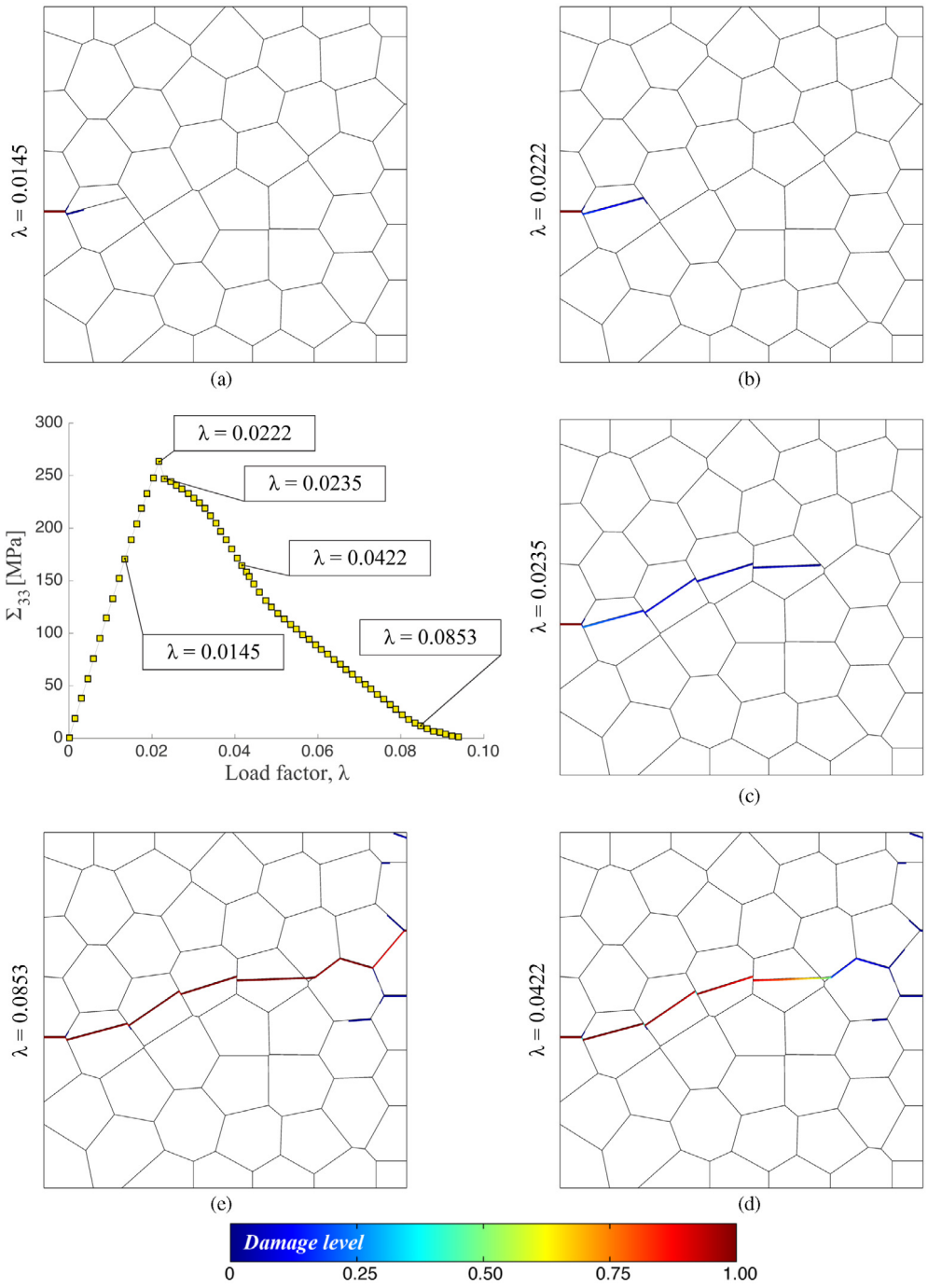

Fig. 11. Micro-cracking patterns of the 50-grain morphology shown in Fig. 8 at different values of the load factor λ. The colourmap denotes the damage level of the inter- and transgranular interfaces. (For interpretation of the references to colour in this figure legend, the reader is referred to the web version of this article.)

$s_{ms} = 2$ μm satisfactorily overlap. The crack pattern at the last computed step is shown in Fig. 14(b) in which, once again, the grains are coloured according to their susceptibility to transgranular cracking. In this case, the angle θ used to compute transgranular susceptibility index $TG(\theta)$ is the second angle of the three Euler angles defining the grains' orientation according to the ZXZ convention. The mesh size $s_{ms} = 3$ μm is then used to perform the tests

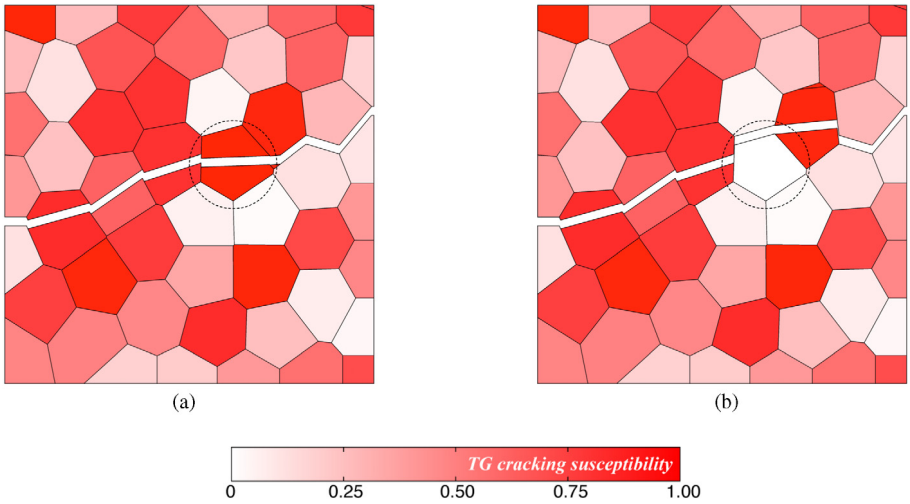

Fig. 12. (a) Fully developed micro-cracking pattern in the 50-grain morphology in Fig. 8; (b) Final micro-cracking pattern of the 50-grain morphology shown in Fig. 8; the circled grain has been rotated to impede the transgranular crack propagation and modify the final crack pattern. The colourmap indicates the grain susceptibility to transgranular cracking. (For interpretation of the references to colour in this figure legend, the reader is referred to the web version of this article.)

that are discussed next, as it represents a satisfactory tradeoff between solution accuracy and number of degrees of freedom.

The same test is then performed on a 100-grain morphology with ASTM grain size $G = 12$ with a pre-existing crack. The morphology, the initial crack and the prescribed boundary conditions are reported in Fig. 15(a). In order to investigate the effect of the fracture toughness ratio γ_G on the macroscopic stress curve, on the micro-crack patterns and micro-damage distribution, the micro-cracking response is computed for two values of the fracture toughness ratio, namely $\gamma_G = 1/4$ and $\gamma_G = 1$.

Fig. 15(b) shows the macroscopic stress response as a function of the load factor λ and the two values of the fracture toughness ratio γ_G. As expected, the fracture toughness ratio γ_G strongly influences the macroscopic stress curve by inducing a drop of the maximum macroscopic stress as it decreases. Fig. 16 reports the cracked morphology for the two considered cases at different levels of the load factor λ. More specifically, Fig. 16(a) corresponds to $\gamma_G = 1/4$ whereas Fig. 16(b) corresponds to $\gamma_G = 1$. In both figures, the left column shows an external view of the morphology at the selected values of the load factor, whereas the right column shows a cut-out view of the morphology at the same load steps, which better highlights the micro-crack propagation through the morphology. In fact, upon colouring the grains according to their susceptibility to transgranular cracking and comparing the internal and the external views, it is observed that the crack propagates as intergranular along the grain boundaries of those grains that are not favourably oriented and as transgranular through those grains that are more susceptible to cleavage micro-cracking.

What discussed above is common between the analyses corresponding to $\gamma_G = 1/4$ and $\gamma_G = 1$. The main difference between the two analyses can be found in the crack patterns and in particular in the damage distribution. In fact, by looking at the first row of Fig. 16(a), (b) and Fig. 17(a), (b), it is possible to see that, for the same load factor, in the morphology with $\gamma_G = 1/4$ the damage has already developed and two transgranular cracks have been introduced whereas, besides the area close to the initial crack tip, the morphology with $\gamma_G = 1$ is almost damage-free.

As soon as the load factor reaches the value $\lambda = 0.0350$, corresponding to the maximum level of macroscopic stress obtained with $\gamma_G = 1$ in Fig. 15(b) and corresponding to the second row of Fig. 16(a), (b) and Fig. 17(a), (b), the crack has fully propagated through the morphology for both values of γ_G. However, for $\gamma_G = 1/4$ the grains that favour the transgranular cracking get cut just one time, whereas for $\gamma_G = 1$ the same grains are cut multiple times. This is due to the morphological constraints of the internal grains in combination with the higher level of stress that needs to be reached in order to induce transgranular damage when $\gamma_G = 1$. Moreover, it is interesting to note that, in Fig. 17(a), the transgranular cracks can be easily distinguished from the intergranular cracks by their higher level of damage for the same load factor as they can withstand a lower level of stress. On the other hand, the damage distribution shown

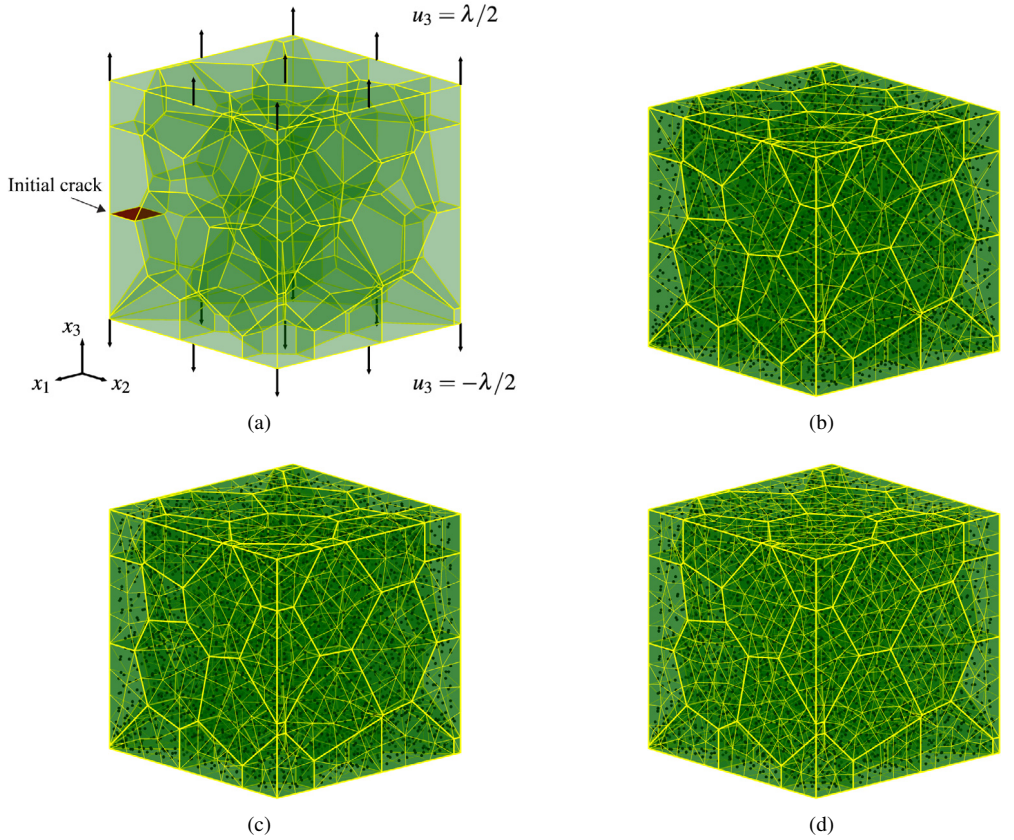

Fig. 13. (a) 50-grain fully 3D polycrystalline morphology with ASTM grain size $G = 12$ subject to prescribed values of vertical displacements u_3 on top and bottom faces. The morphology is also subject to presence of a pre-existing intergranular crack that is highlighted in the figure as a red surface. (b)–(d) Three different meshes of the morphology of Fig. 13(a): (b) $s_{ms} = 4$ μm, (c) $s_{ms} = 3$ μm, (d) $s_{ms} = 2$ μm. In the figures, the black dots denote the volume control points. (For interpretation of the references to colour in this figure legend, the reader is referred to the web version of this article.)

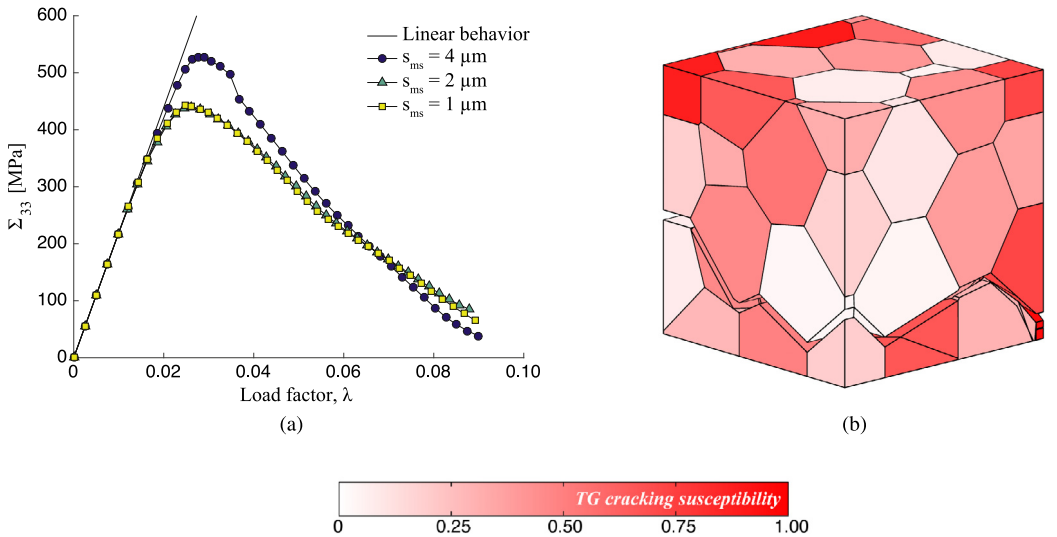

Fig. 14. (a) Macroscopic stress average Σ_{33} as a function of the load factor λ and the different mesh sizes; (b) Final micro-cracking pattern. The colourmap indicates the grain susceptibility to transgranular cracking. (For interpretation of the references to colour in this figure legend, the reader is referred to the web version of this article.)

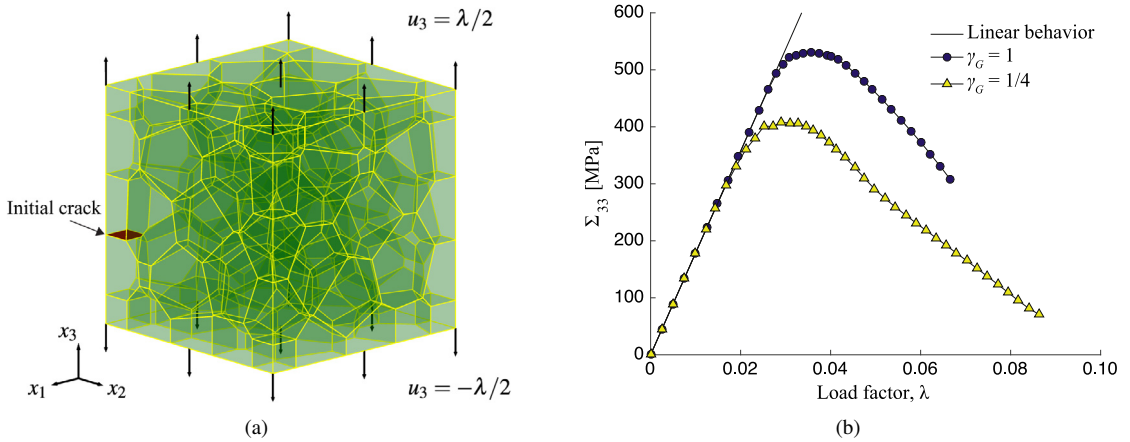

Fig. 15. (a) 100-grain fully 3D polycrystalline morphology with ASTM grain size $G = 12$ subject to prescribed value of vertical displacements u_3 on top and bottom faces. The morphology is also subject to presence of a pre-existing intergranular crack that is indicated in the figure by a red surface. (b) Macroscopic stress average Σ_{33} as a function of the load factor λ and two different values of the fracture toughness ratio γ_G. (For interpretation of the references to colour in this figure legend, the reader is referred to the web version of this article.)

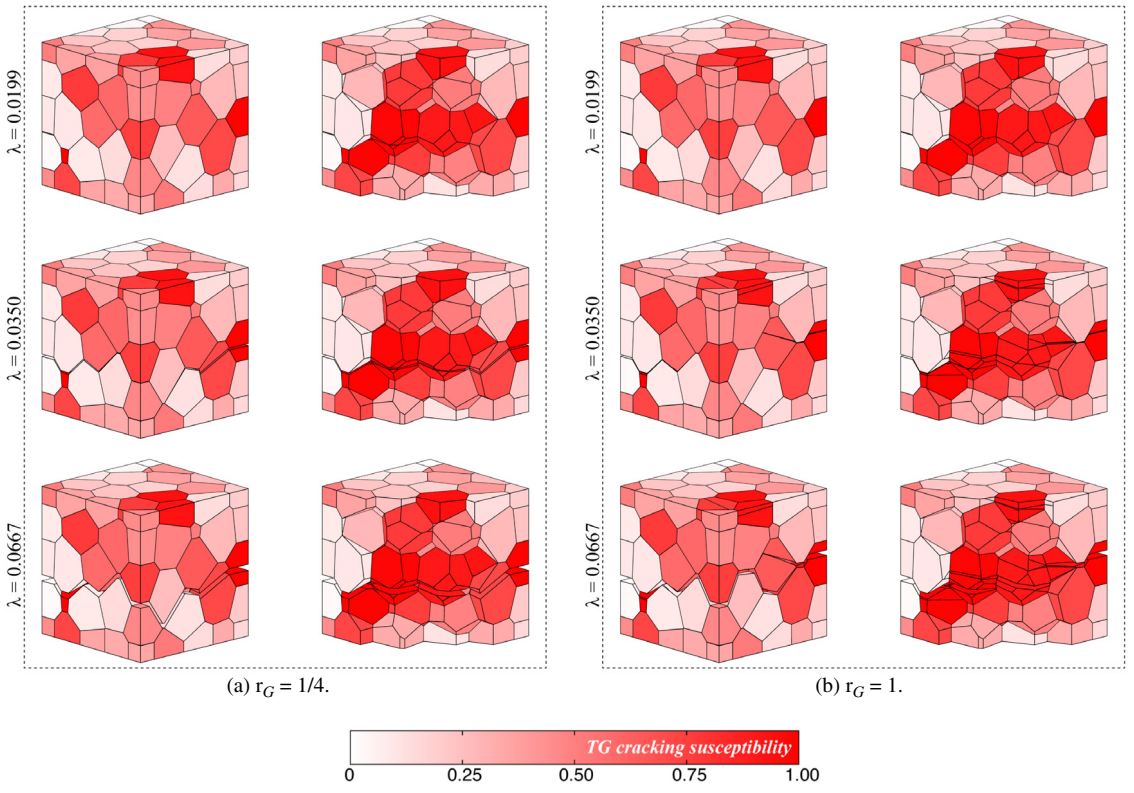

Fig. 16. Micro-cracking patterns of the 100-grain morphology shown in Fig. 15(a) at different values of the load factor λ. (a) $\gamma_G = 1/4$ and (b) $\gamma_G = 1$. In both figures, the left column corresponds to an external view of the morphology whereas the right column corresponds to a cut-out view of the morphology showing the transgranular crack envelope. The colourmap indicates the grain susceptibility to transgranular cracking. (For interpretation of the references to colour in this figure legend, the reader is referred to the web version of this article.)

in Fig. 17(b) is almost uniform among the inter- and transgranular cracks. At this point, the softening has initiated and the damage accumulates over a crack envelope that is well defined.

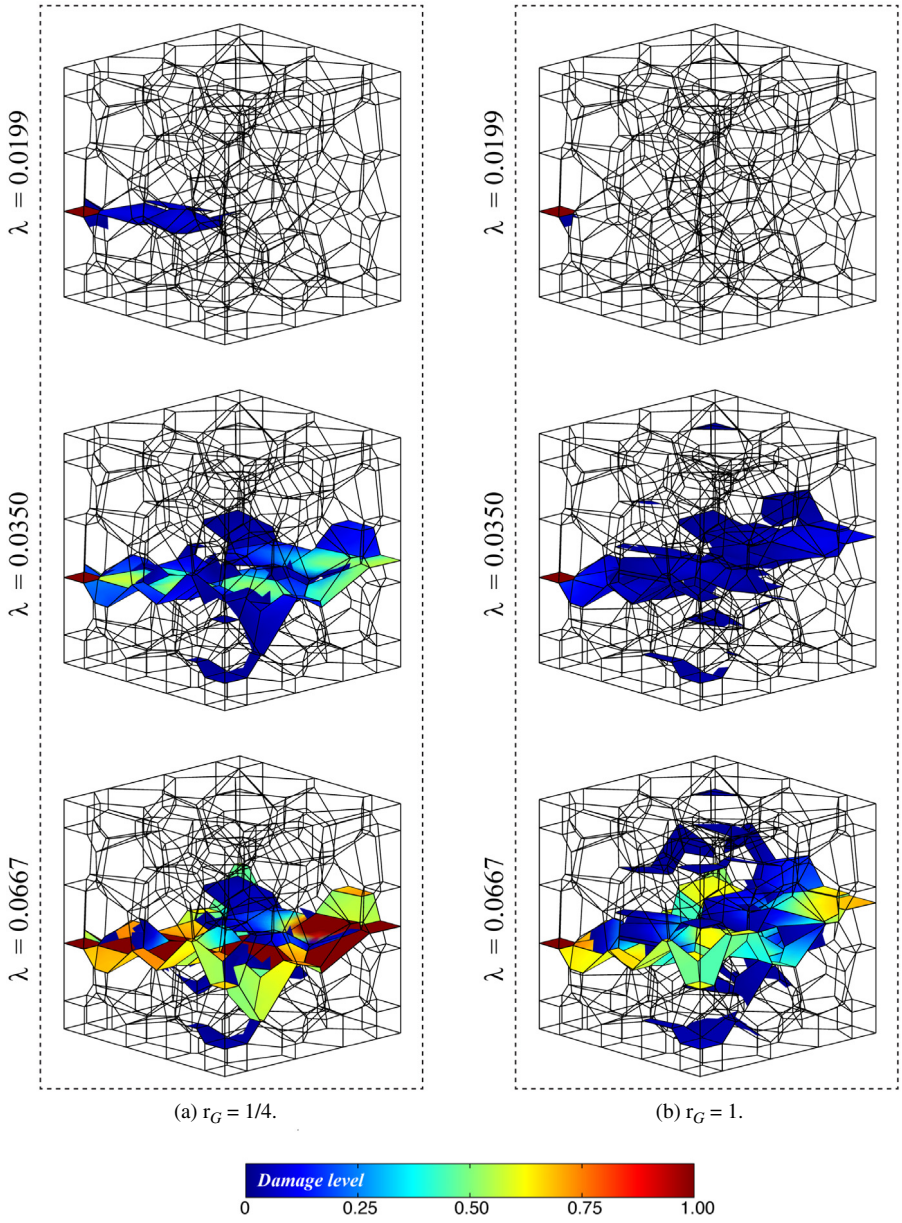

Fig. 17. Damage patterns of the 100-grain morphology shown in Fig. 15(a) at different values of the load factor λ, for fracture toughness ratios of (a) $\gamma_G = 1/4$ and (b) $\gamma_G = 1$. The colourmap denotes the damage level of the inter- and transgranular interfaces. (For interpretation of the references to colour in this figure legend, the reader is referred to the web version of this article.)

In the last set of tests, 100-grain 3D cubic morphologies are subject to micro-cracking without pre-existing damage/crack. The boundary conditions are the same as those in the previous 3D tests, i.e. the morphologies are subject to prescribed value of vertical displacement u_3 on the top and bottom faces of the aggregates, see Fig. 18(a) whereas, on the lateral faces, the normal displacement is set to zero; along the remaining directions, the faces of the aggregates are traction-free. Fig. 18(b) shows the macroscopic stress Σ_{33} as a function of the load factor λ for four different polycrystalline morphologies and for a value of the fracture toughness ratio $\gamma_G = 1$. The four cracked morphologies at a load factor $\lambda = 0.08$ are shown in Fig. 19. The morphologies are coloured according to the grains' susceptibility to transgranular cracking and it can be noted that some suitably oriented grains experience

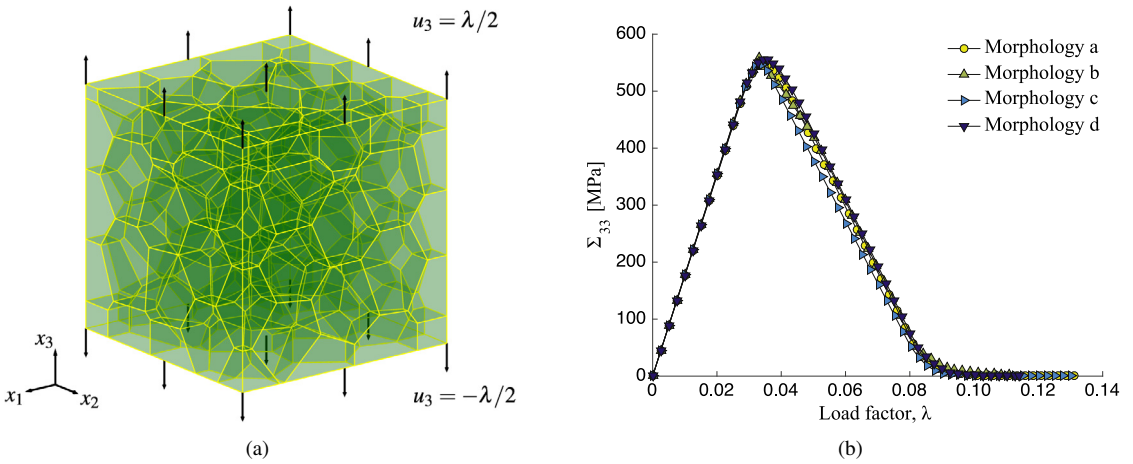

Fig. 18. (a) 100-grain fully 3D polycrystalline morphology with ASTM grain size $G = 12$ subject to prescribed values of vertical displacements u_3 on top and bottom faces. (b) Macroscopic stress average Σ_{33} of the four considered morphologies as a function of the load factor λ.

transgranular cracking during the loading history. However, those micro-cracks do not lead to the generation of the macro-crack of the whole morphology. In fact, the crack pattern of the morphology shown in Fig. 19(a) consists of intergranular micro-cracks only, whereas the damage crack patterns of the morphologies shown in Fig. 19(b), 19(c) and 19(d) are shown in Fig. 20(b), 20(c) and 20(d), respectively. In Fig. 20, the hatched transgranular interfaces are those participating in the generation of the macroscopic crack of the entire morphology. Consistently with the damage distribution reported in Fig. 17(b), the damage level of the morphologies shown in Fig. 20 is almost uniform among inter- and transgranular cracks and mainly depends on the relative orientation between the loading direction and the cracked interfaces.

The same tests have been performed on the morphology shown in Fig. 18(a) for different values of the fracture toughness ratio γ_G, namely $\gamma_G = \infty$, $\gamma_G = 1$ and $\gamma_G = 1/4$. Fig. 21 shows the macroscopic stress Σ_{33} as a function of the load factor λ and the selected values of γ_G. The macroscopic stress curve obtained with $\gamma_G = \infty$ coincides to a purely intergranular failure and the corresponding damage crack pattern is shown in Fig. 22(a). It is interesting to note that the peak value of the macroscopic stress Σ_{33} does not considerably change between the macro curves corresponding $\gamma_G = \infty$ and $\gamma_G = 1$. This is an expected result within the proposed model since, for $\gamma_G = 1$, the cleavage planes represent additional and potential fracture surfaces that do not differ from the grain boundaries in terms of fracture behaviour. On the other hand, reducing the value of γ_G forces the activation of more transgranular surfaces, which fail at a lower level of stress thus inducing a lower peak value in the macroscopic stress Σ_{33}. Reducing the value of γ_G also influences the damage crack patterns of the considered morphology. Figs. 22(b) and 22(c) show the damage crack patterns at a load factor $\lambda = 0.08$. Once again, the transgranular cracks are hatched and it is possible to notice that the number of transgranular cracks corresponding to $\gamma_G = 1/4$ is higher than the number of transgranular cracks corresponding to $\gamma_G = 1$.

4.3. Grain boundary accommodation

To conclude the results section, it is worth noting that the developed model naturally captures the *grain boundary accommodation mechanism*, which is a typical phenomenon experimentally observed in the fracture surfaces of polycrystalline aggregates undergoing inter- and transgranular failure [10–12]. The grain boundary accommodation refers to the initiation and evolution of intergranular damage accompanying the grain-to-grain migration of transgranular cracking over contiguous grains with misaligned crystallographic cleavage systems. From a computational point of view, this mechanism can only be captured by a fully 3D model, as simple 2D models may allow for purely transgranular crack propagation through generally misaligned grains. Within the developed framework, the grain boundary accommodation mechanism naturally occurs in all the presented results, see e.g. Figs. 16, 20 and 22.

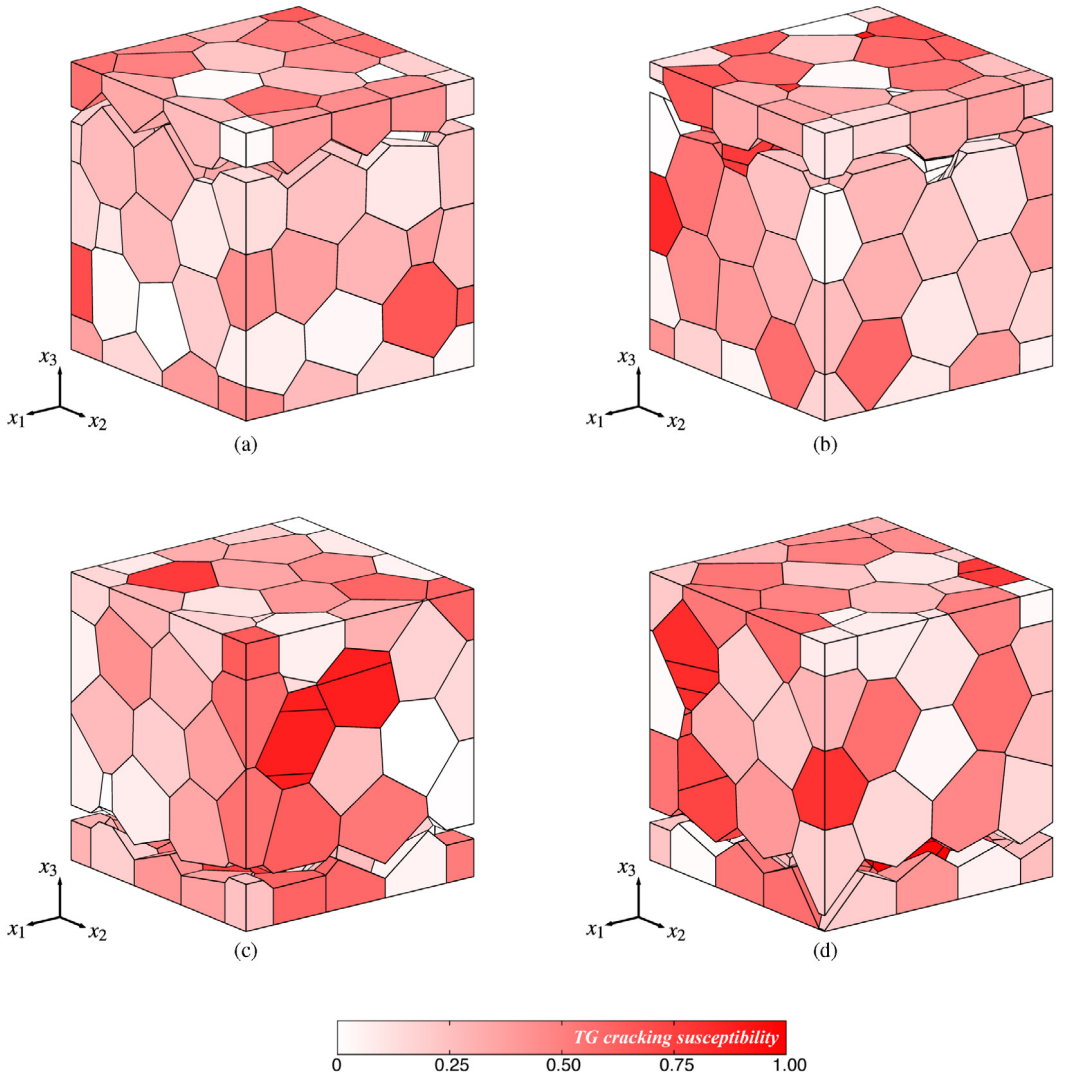

Fig. 19. Micro-cracking patterns of the four considered 100-grain morphologies at the load factor $\lambda = 0.08$. The colourmap indicates the grain susceptibility to transgranular cracking. (For interpretation of the references to colour in this figure legend, the reader is referred to the web version of this article.)

5. Discussion and further developments

Several modelling and computational aspects have been addressed in the present work.

The polycrystalline morphologies are generated using the Voronoi tessellation algorithm through the software library `Voro++` [49]. The inherent statistical variability of polycrystalline morphologies poses a considerable challenge to the generality and robustness of the splitting/remeshing algorithm. `Voro++` has been purposely modified to split and remesh the grains undergoing transgranular failure and the developed algorithm has proved satisfactorily effective and robust.

A development of the proposed model could involve the use of more realistic micro-morphologies, e.g. provided by experimental observations, similar to those used by other authors [3]. The use of more realistic grain representations is possible within the present framework, but it would require a more complex data structure to handle morphology. Moreover, the grains are here modelled as generally anisotropic linear elastic domains: further studies could include the combination of inter and transgranular cracking with other deformation and damage mechanisms such as crystals plasticity [32] or stress corrosion cracking [3,18].

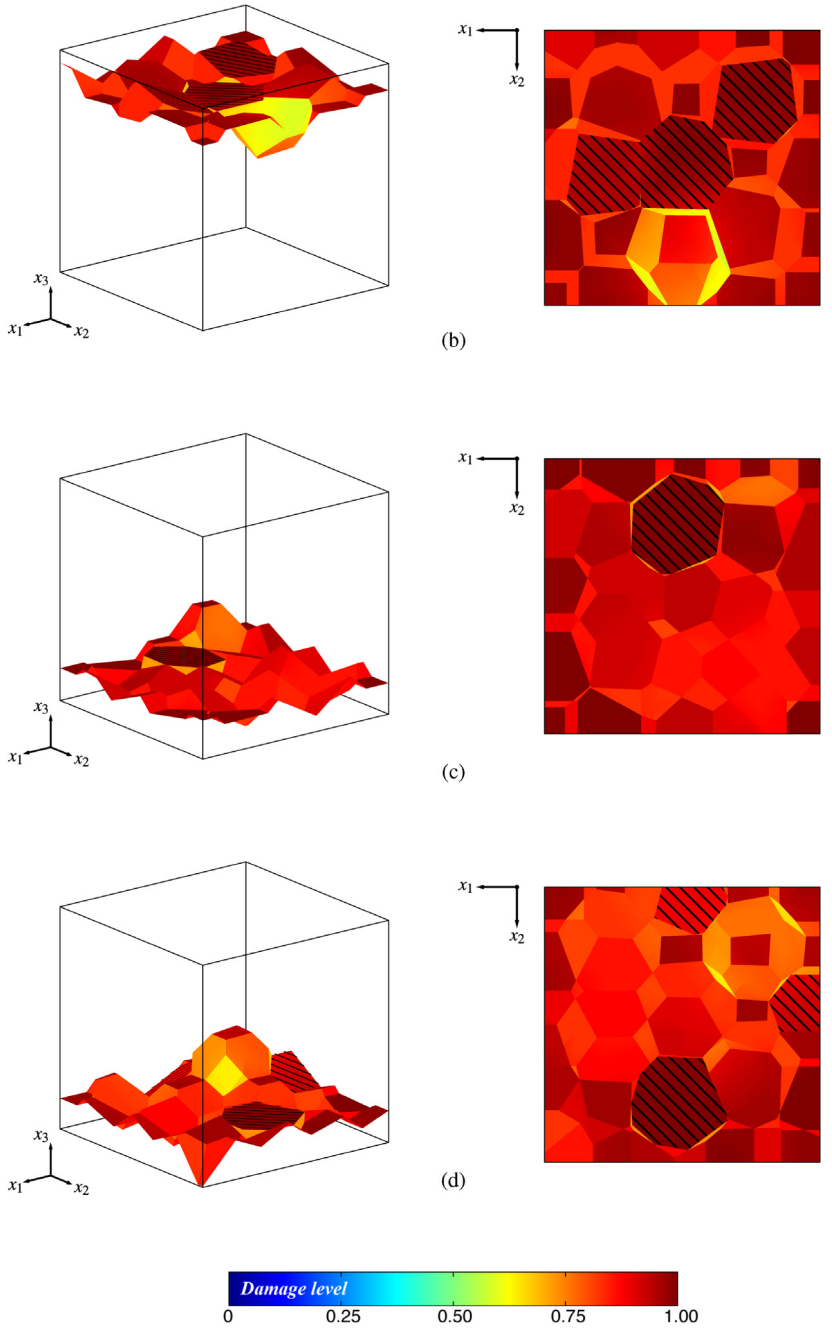

Fig. 20. Figs. (b), (c) and (d) show the damage crack patterns of the morphologies shown in Fig. 19(b), 19(c) and 19(d), respectively. The images on the right show the top view of the damage crack patterns of the figures on the left. In the figures, the transgranular cracks hatched. The colourmap denotes the damage level of the inter- and transgranular interfaces. (For interpretation of the references to colour in this figure legend, the reader is referred to the web version of this article.)

The presented results show that the proposed scheme is able to account for the competition between intergranular and transgranular failure mechanisms and naturally captures and reproduces the grain boundary accommodation occurring in presence of transgranular micro-cracking within polycrystalline aggregates. Additionally, the results show that, by suitably tuning the values of the parameters governing the two fracture mechanisms, it is possible to represent

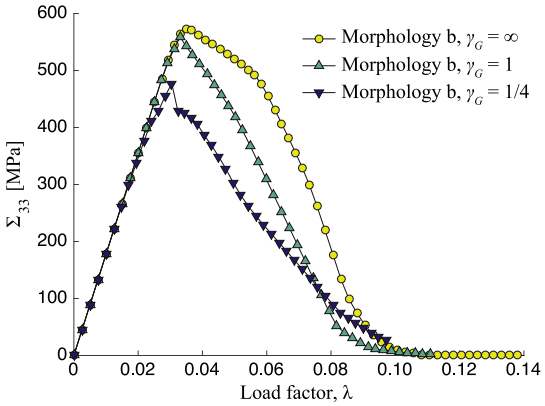

Fig. 21. Macroscopic stress average Σ_{33} of the morphology shown in Fig. 18(a) as a function of the load factor λ and for different values of the fracture toughness ratio γ_G.

different cracking scenarios in terms of inter/transgranular micro-cracking ratios. However a study of the statistical representativity of the micro-cracking response of polycrystalline aggregates subject to inter- and transgranular cracking goes beyond the scope of this paper and a more rigorous investigation of the effects of the micro-mechanics parameters on the averaged macroscopic variables is left for further investigation. To this purpose, the development of computation strategies enabling the analysis of higher numbers of grains could be of relevant interest; the use of fast iterative solvers in conjunction with special matrix formats, i.e. fast multipoles [67] or hierarchical matrices [68–70], could enhance the storage memory and computational time requirements of the implementation.

6. Conclusions

A numerical formulation for intergranular and transgranular micro-cracking in fully 3D polycrystalline materials has been developed, implemented and tested. The competition between inter- and transgranular cracking in three-dimensional anisotropic crystal aggregates has been modelled for the first time in a cohesive grain-boundary framework. Transgranular failure is captured by computing the stress in the interior of the grains and by introducing cohesive cleavage interfaces within the failing grains according to a specific threshold condition. A robust remeshing strategy, taking into account the statistical variability of the polycrystalline morphology, has been developed and implemented, to handle the transgranular grains splitting and propagation. The competition between inter- and transgranular failures has been investigated by varying the fracture energy ratio between the two mechanisms and exploring the effect on both the macro-stress strain curves and the micro-cracking envelope. It has also been shown that the model naturally captures the intergranular grain boundary accommodation to transgranular fracture, which is a phenomenon typically observed in polycrystalline aggregates subjected to inter- and transgranular fracture. The method expresses the polycrystalline problem in terms of grain boundary variables only, thus reducing the computational cost of the simulations. The developed formulation and the implemented code may offer a valuable tool in the study of polycrystalline micro-mechanics.

Acknowledgment

C.H.R. was supported by the Applied Mathematics Program of the U.S. Department of Energy (DOE) Office of Advanced Scientific Computing Research under contract DE-AC02-05CH11231.

Appendix. Anisotropic Green's functions

The 3D Green's functions $G_{ij}(\mathbf{x}, \mathbf{y})$ for anisotropic elasticity are obtained as the solutions of the following problem

$$c_{ikjl} \frac{\partial^2 G_{pj}}{\partial x_k \partial x_l}(\mathbf{x}, \mathbf{y}) + \delta_{pi} \delta(\mathbf{x} - \mathbf{y}) = 0 \tag{A.1}$$

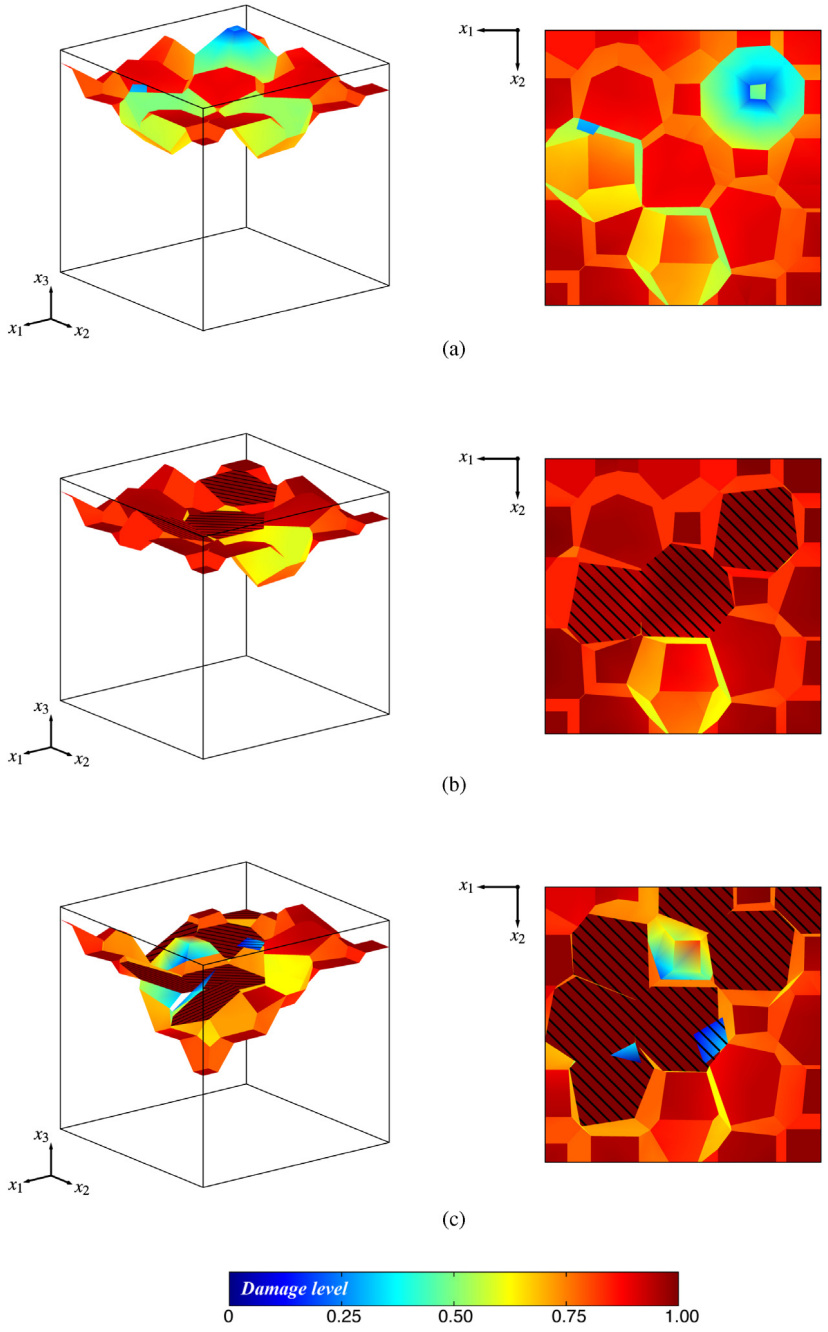

Fig. 22. Damage crack patterns of the morphology shown in Fig. 18(a) for fracture toughness ratios of (a) $\gamma_G = \infty$, (b) $\gamma_G = 1$, and (c) $\gamma_G = 1/4$. The images on the right show the top view of the damage crack patterns of the figures on the left. In the figures, the transgranular cracks are hatched. The colourmap denotes the damage level of the inter- and transgranular interfaces. (For interpretation of the references to colour in this figure legend, the reader is referred to the web version of this article.)

where $\mathbf{y}$ and $\mathbf{x}$ denote the collocation and observation points, respectively, c_{ijkl} is the anisotropic fourth-order elasticity tensor, δ_{pi} denotes the Kronecker delta and $\delta(\mathbf{x} - \mathbf{y})$ the Dirac delta function. By applying the Fourier transform with respect to the variable $\mathbf{x}$ to Eq. (A.1) and following the approach proposed in Ref. [71], the Green's functions $G_{ij}(\mathbf{x}, \mathbf{y})$

and their derivatives can be obtained in terms of spherical harmonics using

$$\frac{\partial^{(I)} G_{ij}}{\partial r_1^{(\alpha_1)} \partial r_2^{(\alpha_2)} \partial r_3^{(\alpha_3)}}(\mathbf{r}) = \frac{1}{4\pi r^{I+1}} \sum_{\ell \in \mathcal{L}}^{\infty} P_\ell^I(0) \sum_{m=-\ell}^{\ell} \widetilde{G}^{\ell,m}_{ij,(\alpha_1,\alpha_2,\alpha_3)} Y_\ell^m(\hat{\mathbf{r}}), \tag{A.2}$$

where $\mathbf{r} \equiv \mathbf{x} - \mathbf{y}$, $r = \sqrt{r_k r_k}$, $\hat{\mathbf{r}} = \mathbf{r}/r$; $I = \alpha_1 + \alpha_2 + \alpha_3$ denotes the order of derivation and $\mathcal{L}$ is the set of positive even (odd) integers when I is even (odd). $P_\ell^I(0)$ is the ℓth associated Legendre polynomials of degree I evaluated at 0 and $Y_\ell^m(\hat{\mathbf{r}})$ is the spherical harmonic of order ℓ and degree m. The coefficients $\widetilde{G}^{\ell,m}_{ij,(\alpha_1,\alpha_2,\alpha_3)}$ of the series are computed using the integral over the unit sphere S_1,

$$\widetilde{G}^{\ell,m}_{ij,(\alpha_1,\alpha_2,\alpha_3)} = \int_{S_1} (\hat{\xi}_1)^{\alpha_1} (\hat{\xi}_2)^{\alpha_2} (\hat{\xi}_3)^{\alpha_3} \widetilde{G}_{ij}(\hat{\xi}) \bar{Y}_\ell^m(\hat{\xi}) \mathrm{d}S(\hat{\xi}), \tag{A.3}$$

where $\widetilde{G}_{ij}(\boldsymbol{\xi}) = \left[c_{ikjl}\xi_k\xi_l\right]^{-1}$ and $\bar{Y}_\ell^m$ the complex conjugate of Y_ℓ^m. The reader is referred to Ref. [71] for further details about the spherical harmonics expansions of the fundamental solutions.

The kernels $U_{ij}(\mathbf{x}, \mathbf{y})$, $T_{ij}(\mathbf{x}, \mathbf{y})$, $U_{ijk}(\mathbf{x}, \mathbf{y})$ and $T_{ijk}(\mathbf{x}, \mathbf{y})$ appearing in Eqs. (1) and (2) are then computed as [41]

$$U_{ij}(\mathbf{x}, \mathbf{y}) = G_{ij}(\mathbf{x}, \mathbf{y}), \quad T_{ij}(\mathbf{x}, \mathbf{y}) = n_k(\mathbf{x}) c_{jkpq} \frac{\partial G_{ip}}{\partial x_q}(\mathbf{x}, \mathbf{y}), \tag{A.4a}$$

$$U_{ijk}(\mathbf{x}, \mathbf{y}) = c_{ijpq} \frac{G_{pk}}{\partial y_q}(\mathbf{x}, \mathbf{y}), \quad T_{ijk}(\mathbf{x}, \mathbf{y}) = n_l(\mathbf{x}) c_{ijrs} c_{klpq} \frac{\partial^2 G_{rs}}{\partial x_q \partial y_s}(\mathbf{x}, \mathbf{y}), \tag{A.4b}$$

where $\mathbf{n}(\mathbf{x}) = \{n_i(\mathbf{x})\}$ is the outward unit vector normal to the boundary at the point $\mathbf{x}$.

References

[1] E.B. Tadmor, R.E. Miller, Modeling Materials: Continuum, Atomistic and Multiscale Techniques, Cambridge University Press, 2011.

[2] I. Benedetti, F. Barbe, Modelling polycrystalline materials: an overview of three-dimensional grain-scale mechanical models, J. Multiscale Model. 5 (01) (2013) 1350002.

[3] I. Simonovski, L. Cizelj, Towards modeling intergranular stress corrosion cracks on grain size scales, Nucl. Eng. Des. 246 (2012) 107–114.

[4] A. King, G. Johnson, D. Engelberg, W. Ludwig, J. Marrow, Observations of intergranular stress corrosion cracking in a grain-mapped polycrystal, Science 321 (5887) (2008) 382–385.

[5] F. Roters, P. Eisenlohr, L. Hantcherli, D.D. Tjahjanto, T.R. Bieler, D. Raabe, Overview of constitutive laws, kinematics, homogenization and multiscale methods in crystal plasticity finite-element modeling: Theory, experiments, applications, Acta Mater. 58 (4) (2010) 1152–1211.

[6] F. Barbe, R. Quey, A numerical modelling of 3D polycrystal-to-polycrystal diffusive phase transformations involving crystal plasticity, Int. J. Plast. 27 (6) (2011) 823–840.

[7] M. Diehl, M. Wicke, P. Shanthraj, F. Roters, A. Brueckner-Foit, D. Raabe, Coupled crystal plasticity–phase field fracture simulation study on damage evolution around a void: Pore shape versus crystallographic orientation, JOM 69 (5) (2017) 872–878.

[8] T.L. Anderson, T. Anderson, Fracture Mechanics: Fundamentals and Applications, CRC press, 2005.

[9] A. Crocker, P. Flewitt, G. Smith, Computational modelling of fracture in polycrystalline materials, Int. Mater. Rev. 50 (2) (2005) 99–125. http://dx.doi.org/10.1179/174328005X14285.

[10] G. Smith, A. Crocker, R. Moskovic, P. Flewitt, Models to describe brittle and ductile fracture in ferritic steels, Phil. Mag. A 82 (17–18) (2002) 3443–3453.

[11] G. Hughes, G. Smith, A. Crocker, P. Flewitt, An examination of the linkage of cleavage cracks at grain boundaries, Mater. Sci. Technol. 21 (11) (2005) 1268–1274.

[12] G.M. Hughes, G.E. Smith, P.E. Flewitt, A. Crocker, The brittle fracture of polycrystalline zinc, in: Proceedings of the Royal Society of London A: Mathematical, Physical and Engineering Sciences, Vol. 463, The Royal Society, 2007, pp. 2129–2151. http://dx.doi.org/10.1098/rspa.2007.1866.

[13] C. McMahon, Hydrogen-induced intergranular fracture of steels, Eng. Fract. Mech. 68 (6) (2001) 773–788.

[14] G. Mori, D. Scherer, S. Schwentenwein, P. Warbichler, Intergranular stress corrosion cracking of copper in nitrite solutions, Corros. Sci. 47 (9) (2005) 2099–2124.

[15] V. Raja, T. Shoji, Stress Corrosion Cracking: Theory and Practice, Elsevier, 2011.

[16] C. Gandhi, M. Ashby, Overview no. 5: Fracture-mechanism maps for materials which cleave: FCC, BCC and HCP metals and ceramics, Acta Metall. 27 (10) (1979) 1565–1602.

[17] C. Verhoosel, M. Gutiérrez, Modelling inter-and transgranular fracture in piezoelectric polycrystals, Eng. Fract. Mech. 76 (6) (2009) 742–760. http://dx.doi.org/10.1016/j.engfracmech.2008.07.004.

[18] A. Musienko, G. Cailletaud, Simulation of inter-and transgranular crack propagation in polycrystalline aggregates due to stress corrosion cracking, Acta Mater. 57 (13) (2009) 3840–3855. http://dx.doi.org/10.1016/j.actamat.2009.04.035.

[19] S.M.T. Mousavi, B. Hosseinkhani, C. Vieillard, M. Chambart, P.J.J. Kok, J.-F. Molinari, On the influence of transgranular and intergranular failure mechanisms during dynamic loading of silicon nitride, Acta Mater. 67 (2014) 239–251.

[20] S.T. Mousavi, N. Richart, C. Wolff, J.-F. Molinari, Dynamic crack propagation in a heterogeneous ceramic microstructure, insights from a cohesive model, Acta Mater. 88 (2015) 136–146.
[21] L. Lin, X. Wang, X. Zeng, The role of cohesive zone properties on intergranular to transgranular fracture transition in polycrystalline solids, Int. J. Damage Mech. 26 (3) (2015) 379–394.
[22] R. Kraft, J. Molinari, A statistical investigation of the effects of grain boundary properties on transgranular fracture, Acta Mater. 56 (17) (2008) 4739–4749. http://dx.doi.org/10.1016/j.actamat.2008.05.036.
[23] N. Sukumar, D. Srolovitz, T. Baker, J.-H. Prévost, Brittle fracture in polycrystalline microstructures with the extended finite element method, Internat. J. Numer. Methods Engrg. 56 (14) (2003) 2015–2037. http://dx.doi.org/10.1002/nme.653.
[24] D. Wang, J. Zhao, Y. Zhou, X. Chen, A. Li, Z. Gong, Extended finite element modeling of crack propagation in ceramic tool materials by considering the microstructural features, Comput. Mater. Sci. 77 (2013) 236–244. http://dx.doi.org/10.1016/j.commatsci.2013.04.045.
[25] C. Prakash, H. Lee, M. Alucozai, V. Tomar, An analysis of the influence of grain boundary strength on microstructure dependent fracture in polycrystalline tungsten, Int. J. Fract. 199 (1) (2016) 1–20.
[26] M. Ghajari, L. Iannucci, P. Curtis, A peridynamic material model for the analysis of dynamic crack propagation in orthotropic media, Comput. Methods Appl. Mech. Engrg. 276 (2014) 431–452. http://dx.doi.org/10.1016/j.cma.2014.04.002.
[27] H. Chen, Y. Jiao, Y. Liu, Investigating the microstructural effect on elastic and fracture behavior of polycrystals using a nonlocal lattice particle model, Mater. Sci. Eng. A 631 (2015) 173–180. http://dx.doi.org/10.1016/j.msea.2015.02.046.
[28] G. Geraci, M. Aliabadi, Micromechanical boundary element modelling of transgranular and intergranular cohesive cracking in polycrystalline materials, Eng. Fract. Mech. 176 (2017) 351–374.
[29] A. Abdollahi, I. Arias, Numerical simulation of intergranular and transgranular crack propagation in ferroelectric polycrystals, Int. J. Fract. 174 (1) (2012) 3–15. http://dx.doi.org/10.1007/s10704-011-9664-0.
[30] A. Abdollahi, I. Arias, Three-dimensional simulation of crack propagation in ferroelectric polycrystals: Effect of combined toughening mechanisms, Acta Mater. 65 (2014) 106–117. http://dx.doi.org/10.1016/j.actamat.2013.11.016.
[31] J. Clayton, J. Knap, Phase field modeling of directional fracture in anisotropic polycrystals, Comput. Mater. Sci. 98 (2015) 158–169. http://dx.doi.org/10.1016/j.commatsci.2014.11.009.
[32] J. Clayton, J. Knap, Phase field modeling and simulation of coupled fracture and twinning in single crystals and polycrystals, Comput. Methods Appl. Mech. Engrg. (2016) 447–467. http://dx.doi.org/10.1016/j.cma.2016.01.023.
[33] P. Shanthraj, B. Svendsen, L. Sharma, F. Roters, D. Raabe, Elasto-viscoplastic phase field modelling of anisotropic cleavage fracture, J. Mech. Phys. Solids 99 (2016) 19–34.
[34] T.-T. Nguyen, J. Rethore, J. Yvonnet, M.-C. Baietto, Multi-phase-field modeling of anisotropic crack propagation for polycrystalline materials, Comput. Mech. 60 (2) (2017) 289–314.
[35] A. Shterenlikht, L. Margetts, Three-dimensional cellular automata modelling of cleavage propagation across crystal boundaries in polycrystalline microstructures, in: Proc. R. Soc. A, Vol. 471, The Royal Society, 2015, p. 20150039.
[36] D. di Caprio, J. Stafiej, G. Luciano, L. Arurault, 3D cellular automata simulations of intra and intergranular corrosion, Corros. Sci. 112 (2016) 438–450.
[37] G. Sfantos, M. Aliabadi, A boundary cohesive grain element formulation for modelling intergranular microfracture in polycrystalline brittle materials, Internat. J. Numer. Methods Engrg. 69 (8) (2007) 1590–1626. http://dx.doi.org/10.1002/nme.1831.
[38] I. Benedetti, M. Aliabadi, A three-dimensional grain boundary formulation for microstructural modeling of polycrystalline materials, Comput. Mater. Sci. 67 (2013) 249–260. http://dx.doi.org/10.1016/j.commatsci.2012.08.006.
[39] I. Benedetti, M. Aliabadi, A three-dimensional cohesive-frictional grain-boundary micromechanical model for intergranular degradation and failure in polycrystalline materials, Comput. Methods Appl. Mech. Engrg. 265 (2013) 36–62. http://dx.doi.org/10.1016/j.cma.2013.05.023.
[40] V. Gulizzi, A. Milazzo, I. Benedetti, An enhanced grain-boundary framework for computational homogenization and micro-cracking simulations of polycrystalline materials, Comput. Mech. 56 (4) (2015) 631–651. http://dx.doi.org/10.1007/s00466-015-1192-8.
[41] I. Benedetti, V. Gulizzi, V. Mallardo, A grain boundary formulation for crystal plasticity, Int. J. Plast. 83 (2016) 202–224. http://dx.doi.org/10.1016/j.ijplas.2016.04.010.
[42] G. Sfantos, M. Aliabadi, Multi-scale boundary element modelling of material degradation and fracture, Comput. Methods Appl. Mech. Engrg. 196 (7) (2007) 1310–1329. http://dx.doi.org/10.1016/j.cma.2006.09.004.
[43] I. Benedetti, M. Aliabadi, Multiscale modeling of polycrystalline materials: A boundary element approach to material degradation and fracture, Comput. Methods Appl. Mech. Engrg. 289 (2015) 429–453. http://dx.doi.org/10.1016/j.cma.2015.02.018.
[44] G. Voronoï, Nouvelles applications des paramètres continus à la théorie des formes quadratiques. Deuxième mémoire. Recherches sur les parallélloèdres primitifs., J. Reine Angew. Math. 134 (1908) 198–287.
[45] Z. Fan, Y. Wu, X. Zhao, Y. Lu, Simulation of polycrystalline structure with Voronoi diagram in Laguerre geometry based on random closed packing of spheres, Comput. Mater. Sci. 29 (3) (2004) 301–308.
[46] C. Lautensack, Fitting three-dimensional Laguerre tessellations to foam structures, J. Appl. Stat. 35 (9) (2008) 985–995.
[47] F. Fritzen, T. Böhlke, E. Schnack, Periodic three-dimensional mesh generation for crystalline aggregates based on Voronoi tessellations, Comput. Mech. 43 (5) (2009) 701–713.
[48] R. Quey, P.R. Dawson, F. Barbe, Large scale 3D random polycrystals for the finite element method: Generation, meshing and remeshing, Comput. Methods Appl. Mech. Engrg. 200 (17) (2011) 1729–1745.
[49] C.H. Rycroft, Voro++: A three-dimensional Voronoi cell library in C++, Chaos 19 (2009) 041111.
[50] P. Banerjee, The Boundary Element Methods in Engineering, McGraw-Hill, 1994, pp. 177–188.
[51] M. Aliabadi, The Boundary Element Method: Applications in Solids and Structures, Vol. 2, Wiley, Chicester, 2002.
[52] V. Tvergaard, Effect of fibre debonding in a whisker-reinforced metal, Mater. Sci. Eng. A 125 (2) (1990) 203–213.
[53] X.-P. Xu, A. Needleman, Numerical simulations of dynamic crack growth along an interface, Int. J. Fract. 74 (4) (1996) 289–324.

[54] G.T. Camacho, M. Ortiz, Computational modelling of impact damage in brittle materials, Internat. J. Solids Structures 33 (20) (1996) 2899–2938. http://dx.doi.org/10.1016/0020-7683(95)00255-3.
[55] M. Ortiz, A. Pandolfi, Finite-deformation irreversible cohesive elements for three-dimensional crack-propagation analysis, Internat. J. Numer. Methods Engrg. 44 (9) (1999) 1267–1282. http://dx.doi.org/10.1002/(SICI)1097-0207(19990330)44:9<1267::AID-NME486>3.0.CO;2-7.
[56] H.D. Espinosa, P.D. Zavattieri, A grain level model for the study of failure initiation and evolution in polycrystalline brittle materials. Part I: Theory and numerical implementation, Mech. Mater. 35 (3) (2003) 333–364.
[57] H.D. Espinosa, P.D. Zavattieri, A grain level model for the study of failure initiation and evolution in polycrystalline brittle materials. Part II: numerical examples, Mech. Mater. 35 (3) (2003) 365–394.
[58] V. Tomar, J. Zhai, M. Zhou, Bounds for element size in a variable stiffness cohesive finite element model, Internat. J. Numer. Methods Engrg. 61 (11) (2004) 1894–1920.
[59] J. Riedle, P. Gumbsch, H.F. Fischmeister, Cleavage anisotropy in tungsten single crystals, Phys. Rev. Lett. 76 (19) (1996) 3594.
[60] S. Kumar, W.A. Curtin, Crack interaction with microstructure, Mater. Today 10 (9) (2007) 34–44.
[61] M. Joo, D.-W. Suh, J. Bae, H. Bhadeshia, Role of delamination and crystallography on anisotropy of Charpy toughness in API-X80 steel, Mater. Sci. Eng. A 546 (2012) 314–322.
[62] S. Ii, C. Iwamoto, K. Matsunaga, T. Yamamoto, Y. Ikuhara, TEM in situ observation of fracture behavior in ceramic materials, Appl. Surf. Sci. 241 (1) (2005) 68–74.
[63] J.R. Rice, Mathematical analysis in the mechanics of fracture, in: Fracture: an Advanced Treatise, Vol. 2, 1968, pp. 191–311.
[64] O. Schenk, A. Wächter, M. Hagemann, Matching-based preprocessing algorithms to the solution of saddle-point problems in large-scale nonconvex interior-point optimization, Comput. Optim. Appl. 36 (2–3) (2007) 321–341.
[65] O. Schenk, M. Bollhöfer, R.A. Römer, On large-scale diagonalization techniques for the Anderson model of localization, SIAM Rev. 50 (1) (2008) 91–112.
[66] A. Kuzmin, M. Luisier, O. Schenk, Fast methods for computing selected elements of the greens function in massively parallel nanoelectronic device simulations, in: European Conference on Parallel Processing, Springer, 2013, pp. 533–544.
[67] Y. Liu, Fast Multipole Boundary Element Method: Theory and Applications in Engineering, Cambridge university press, 2009.
[68] M. Bebendorf, Hierarchical Matrices: a Means to Efficiently Solve Elliptic Boundary Value Problems, Vol. 63, Springer Science & Business Media, 2008.
[69] I. Benedetti, M. Aliabadi, G. Davi, A fast 3D dual boundary element method based on hierarchical matrices, Int. J. Solids Struct. 45 (7) (2008) 2355–2376.
[70] I. Benedetti, A. Milazzo, M. Aliabadi, A fast dual boundary element method for 3D anisotropic crack problems, Internat. J. Numer. Methods Engrg. 80 (10) (2009) 1356–1378.
[71] V. Gulizzi, A. Milazzo, I. Benedetti, Fundamental solutions for general anisotropic multi-field materials based on spherical harmonics expansions, Int. J. Solids Struct. 100 (2016) 169–186. http://dx.doi.org/10.1016/j.ijsolstr.2016.08.014.